ACS APPLIED MATERIALS & INTERFACES

www.acsami.org

Research Article

# Extending the Bioavailability of Hydrophilic Antioxidants for Metal Ion Detoxification via Crystallization with Polysaccharide Dopamine

Ryan Miller, Youngsam Kim, Chang Gyun Park, Chris Torres, Byoungsoo Kim, Jonghwi Lee, David Flaherty, Hee-Sun Han, Young Jun Kim,* and Hyunjoon Kong*

Cite This: *ACS Appl. Mater. Interfaces* 2022, 14, 39759–39774

Read Online

ACCESS | Metrics & More | Article Recommendations | Supporting Information

**ABSTRACT:** Although metal ions, such as silver and gold, have been shown to have strong antimicrobial properties, their potential to have toxic effects on human and environmental health has gained interest with an improved understanding of their mechanisms to promote oxidative stress. Redox control is a major focus of many drug delivery systems and often incorporates an antioxidant as the active pharmaceutical ingredient (API) to neutralize overproduced reactive oxygen species (ROS). Nevertheless, there are still limitations with bioavailability and extended redox control with regard to antioxidant drug delivery. Herein, this study develops a colloidal antioxidant crystal system that dissolves sustainably through polymer stabilization using sodium hyaluronate conjugated with dopamine (HA-dopa). We explore the role of dopamine incorporation into crystal-stabilizing polymers and quantify the balance between drug–polymer interactions and competing polymer–polymer interactions. We propose that this type of analysis is useful in the engineering of and provides insight into the release behavior of polymer–crystal complexes. In developing our crystal complex, *N*-acetylcysteine (NAC) was used as the model antioxidant to protect against silver ion toxicity. We found that our optimized HA-dopa-stabilized NAC crystals prolong the release time of NAC 5-fold compared to a polymer-free NAC crystal. Therefore, following sublethal exposure to $AgNO_3$, the extended lifetime of NAC was able to maintain normal intracellular ROS levels, modulate metabolic function, mitigate fluctuations in ATP levels and ATP synthase activity, and preserve contraction frequency in engineered cardiac muscle tissue. Furthermore, the protective effects of the HA-dopa-stabilized NAC crystals were extended to a *Daphnia magna* model where silver-ion-induced change to both cell-level biochemistry and organ function was alleviated. As such, we propose that the packaging of hydrophilic antioxidants as colloidal crystals drastically extends the lifetime of the API, better maintains ROS homeostasis post metal ion exposure, and therefore preserves both intracellular biochemistry and tissue functionality.

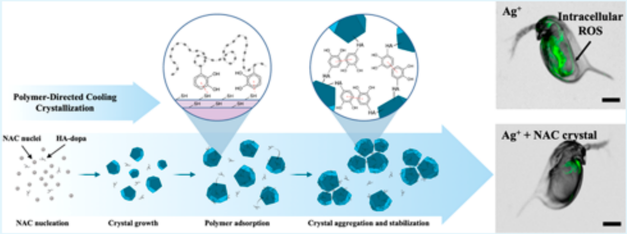

**KEYWORDS:** *cardiomyocytes, daphnia, drug crystallization, N-acetylcysteine, oxidative stress, silver nanoparticles*

## 1. INTRODUCTION

Silver nanoparticles (AgNPs) have strong antimicrobial and antiviral properties and are processed into various forms for household products, agricultural and industrial applications, medical devices, and therapeutic treatments.[1−4] More specifically, in healthcare, AgNPs have been added to the formulations for disinfectants as well as wound dressings and have been shown to prevent bacterial colonization that can lead to infection, inflammation, impaired wound healing, and in extreme cases death.[2−6] The antimicrobial nature of AgNPs leads to many promising applications, albeit studies have identified silver-ion release as toxic to both ecological systems and humans.[3−12] As the use of nanosilver becomes more common place, it is important to consider the implications on intracellular biochemistry and macroscale tissue behavior. Many studies have explored the basis of AgNP toxicity, and while several mechanisms exist, a change in the cell's oxidative state is a principal component of silver-ion toxicity. Intracellular oxidative stress triggered by the overproduction of reactive oxygen species (ROS) is in part caused by silver-ion disruption of mitochondrial function.[5,11−14] Silver ions can also deactivate endogenous antioxidants through protein conformational changes, such as with catalase, or binding to active sulfur groups, such as with reduced glutathione and superoxide dismutase (SOD).[11,12]

ROS are inevitable byproducts of cellular respiration and when maintained at normal physiological levels mediate the intracellular signaling responsible for the regulation of cell adhesion, proliferation, differentiation, senescence, and apoptosis.[15−20] Furthermore, balanced ROS levels are necessary for proper stimulation of tissue-forming cells and immune cells

Received: May 18, 2022
Accepted: August 11, 2022
Published: August 25, 2022

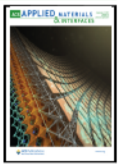

https://doi.org/10.1021/acsami.2c08889

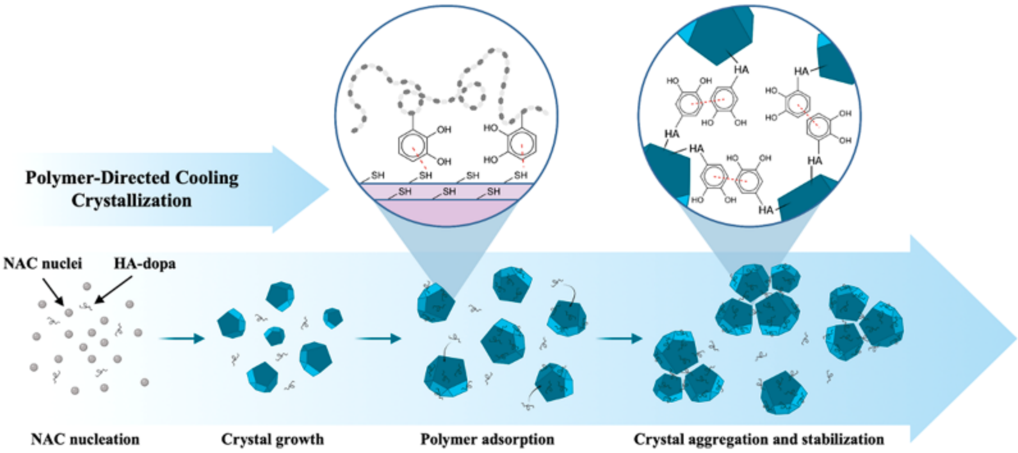

**Figure 1.** Schematic of the NAC crystallization process in the presence of HA-dopa.

responsible for enhanced wound healing.[20−24] However, the overproduction of ROS commonly caused by proinflammatory cytokine signaling, pathogenic bacterial infections, dysfunction of the mitochondria, and suppression of antioxidant signaling can be problematic for normal cellular function.[25−28] The prolonged survival of these reactive species can denature lipids, nucleic acids, and proteins through various oxidative pathways. In the case of cardiac tissue, deviations in adenosine triphosphate (ATP) levels are directly related to abnormal myofilament contraction and relaxation frequencies.[29] Therefore, to maintain a physiological balance of ROS, cells have a sophisticated antioxidant regulatory system; however, silver-ion-induced disruption in homeostasis can overwhelm endogenous antioxidant defenses and result in inadequate scavenging of ROS.

In order to recover balanced ROS activities, exogenous antioxidants are administered to directly scavenge ROS or stimulate the production of antioxidant enzymes by cells.[18,30−33] Many of these antioxidant drugs are hydrophobic and have poor bioavailability because of their reduced solubility in aqueous environments. As such, polymeric additives can be used to fabricate amorphic solid dispersions (ASDs) of hydrophobic antioxidants to partially improve the bioavailability.[34−36] Alternatively, hydrophilic antioxidants are a promising candidate because of their high solubility in tissue fluid. However, their merits are offset by rapid metabolism and fast diffusion from oxidative tissue, leading to both a reduced lifetime and the need for increased or more frequent dosing.[18,32] In general, hydrophilic antioxidants in the soluble state can lose their activities within 24 h *in vitro* and 12 h *in vivo*. As such, efforts have been made to extend the working time of hydrophilic antioxidants without altering their chemical structure and sacrificing bioavailability. One popular approach is to encapsulate antioxidants into biodegradable nano- or microsized carriers. These can be of polymeric forms or lipid forms, and many studies have shown promising results in extended antioxidant release kinetics and drug residence time.[32,37−41] Alternatively, hydrophilic antioxidants can be dosed in the crystalline form to extend the release time and increase the lifetime of antioxidant activity. However, in the case of extremely hydrophilic antioxidants, pure crystalline forms dissolve in a few hours and could benefit from a coupled approach to release.

To this end, this study demonstrates that hydrophilic antioxidant crystals complexed with polymeric additives show greatly improved efficacy in protecting tissue from silver-ion-induced oxidative stress compared to polymer-free antioxidant crystals. We took inspiration from the approach to forming ASDs, but rather than the polymeric excipients preventing ripening and crystal formation, when complexed with hydrophilic drugs, they promote increased crystal stability through a combination of mechanisms. First, we propose that engineered polymeric excipients with high affinity for crystal surface adsorption may inhibit dissolution through desolvation of the crystal surface. Second, functional moieties designed to facilitate polymer−polymer interactions can be used to drive crystal aggregation and result in a decrease in the dissolution rate of the aggregate core. As such, we hypothesized that crystallization of antioxidants with sodium hyaluronate (HA) conjugated with controlled numbers of dopamine (HA-dopa) would extend the period during which antioxidants are able to retain or restore ROS balance from an oxidative environment due to sustained antioxidant release (Figure 1). Specifically, the dopamine groups tethered to HA molecules facilitate two types of interactions: (1) thermodynamically driven association with antioxidants leading to HA-induced desolvation of antioxidants and (2) $\pi-\pi$ stacking and hydrogen bonding between neighboring polymers, leading to crystal aggregation.

We examined our hypothesis by using *N*-acetylcysteine (NAC) as the model hydrophilic antioxidant. NAC is commonly used to promote intracellular glutathione (GSH) synthesis that scavenges ROS and regenerates other antioxidants such as tocopherols and ascorbate.[42−44] In order to explore the ability of our polymer-assembled NAC crystals to remediate normal intracellular biochemistry and tissue function following acute AgNO$_3$ exposure, we established two distinct *in vitro* cardiac models. Cardiac muscle sheets derived from rat cardiomyoblasts and human cardiomyocytes were used to contextualize silver-ion implications on both animal and human health. To expand the protective effects of the crystal on the biological processes from cellular function to attenuated heart function, *Daphnia magna* were used as an *in vivo* model. The crystals were orally administered by the daphnid's specific filter-feeding capabilities after silver-ion exposure. Due to the daphnid's open blood circulatory system, the heart can be exposed to both silver ions and NAC molecules. This *in vivo* model is particularly useful as a means to study environmental impacts from silver-ion exposure but also to probe human cardiotoxicity due to their myogenic heart which is similar to the human heart.[45−48] With these *in vitro*

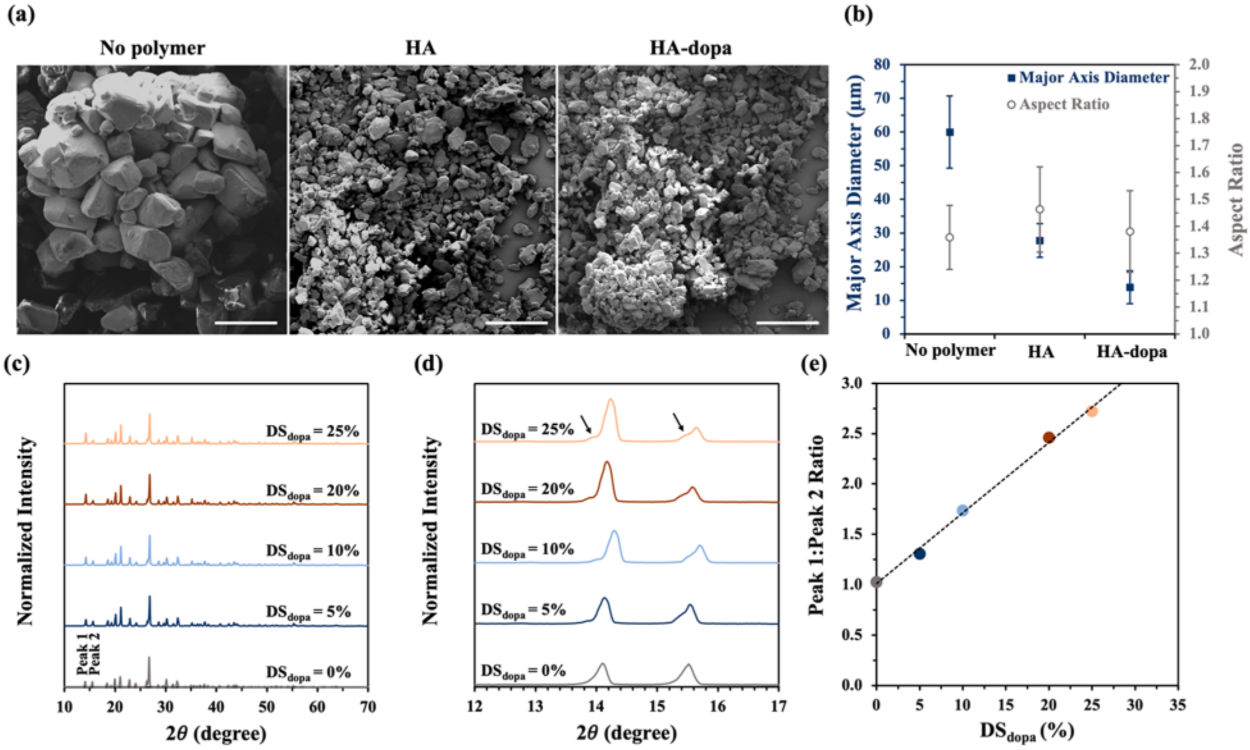

**Figure 2.** Characterization of NAC crystallinity in the presence of HA-dopa. (a) SEM image of pure NAC crystal, NAC crystallized with HA, and NAC crystallized with HA-dopa ($DS_{dopa}$ = 20%). Scale bar = 100 μm. (b) Analysis of major axis diameter (blue square) and aspect ratio (gray circle) of NAC crystals. Each data point and error bar represent average and 95% confidence intervals of five different samples per condition. (c) XRD patterns of NAC crystals. (d) XRD peaks 1 and 2 for NAC crystals. Arrows depict observable peak broadening. (e) Ratio of integrated XRD peak 1 and peak 2 for NAC crystals.

and *in vivo* platforms, we measured the extent to which our NAC/HA-dopa crystal complex serves to avoid aberrant biochemistry and physiological function through the characterization of metabolic activity, intracellular ROS levels, adenosine triphosphate (ATP) and ATP synthase activities, superoxide dismutase (SOD) levels, and beating behavior.

## 2. RESULTS AND DISCUSSION

**2.1. Characterization of HA-dopamine.** In this study, sodium hyaluronate (HA), a hydroscopic biopolymer, was used as the base polymer to induce polymer-directed crystallization of *N*-acetylcysteine (NAC). Since the crystalline structure of NAC is influential to the dissolution kinetics, we used a high molecular weight ($M_n \sim 600$ kDa) form of HA to minimize polymer incorporation into the crystalline structure. As such, HA could act as either a site for NAC nucleation or adsorb to the surface of the NAC crystal during crystal growth. To further increase the association between NAC and polymer, HA was conjugated with dopamine. Dopamine-conjugated HA (HA-dopa) was synthesized by forming an amide bond between the carboxylic acid on HA and the primary amine of dopamine using conventional carbodiimide chemistry. To minimize polydopamine formation, this reaction was conducted in acidic conditions.

To validate successful conjugation of dopamine to HA, we ran $^1$H NMR (600 MHz) for HA and HA-dopa in deuterium oxide (Figures S1−2). Furthermore, $^1$H NMR was used to characterize the degree of substitution of dopamine to HA ($DS_{dopa}$). $DS_{dopa}$ is defined as the percentage of carboxylic acid groups on HA converted to amide bonds with dopamine. The aromatic proton peaks on the dopamine moieties were observed at 6.55−7.1 ppm, and the methyl ketone proton peaks on HA were observed at 1.83 ppm (labeled characteristic peak "a"). The hydrogen atoms on the first carbon from the amide on conjugated dopamine were shifted to 2.71−2.75 ppm and labeled as characteristic peak "b". According to the integration of the characteristic peak intensities (Table S1), $DS_{dopa}$ could be varied from 5% to 10%, 20%, and 25% by altering the molar ratio of dopamine to sodium glucuronate of HA from 2:9 to 4:9, 8:9, and 10:9, respectively.

To further confirm the successful conjugation of dopamine to HA through the formation of a secondary amide bond, we drop cast either HA or HA-dopa thin films on CaF windows and ran FTIR spectroscopy under He flow (Figure S3a). When comparing the spectra of the two different polymer films, we identified two distinct regions where the peak intensities shift. The first region spans 1500−1750 cm$^{-1}$, and there are four observable peaks. The peak at 1617.6 cm$^{-1}$ represents the signal from the secondary amide bonds; the peak at 1653.6 cm$^{-1}$ marks carboxylic acid dimers; and the peak at 1733.3 cm$^{-1}$ describes carboxylic acid monomers. Although HA has a secondary amide functional group in the monomer, the intensity of this peak is larger for HA-dopa. This increase corresponds to the formation of a secondary amide following conjugation with each dopamine molecule. Moreover, we see a proportional decrease in the intensity of the carboxylic acid dimers (1653.6 cm$^{-1}$) for HA-dopa. We also see the formation of carboxylic acid monomer peaks (1733.3 cm$^{-1}$) that are blue-shifted from the carboxylic acid dimers in the HA-dopa thin film. Dopamine saturation of the carboxylic acids on HA decreases the likelihood of two carboxylic acids forming

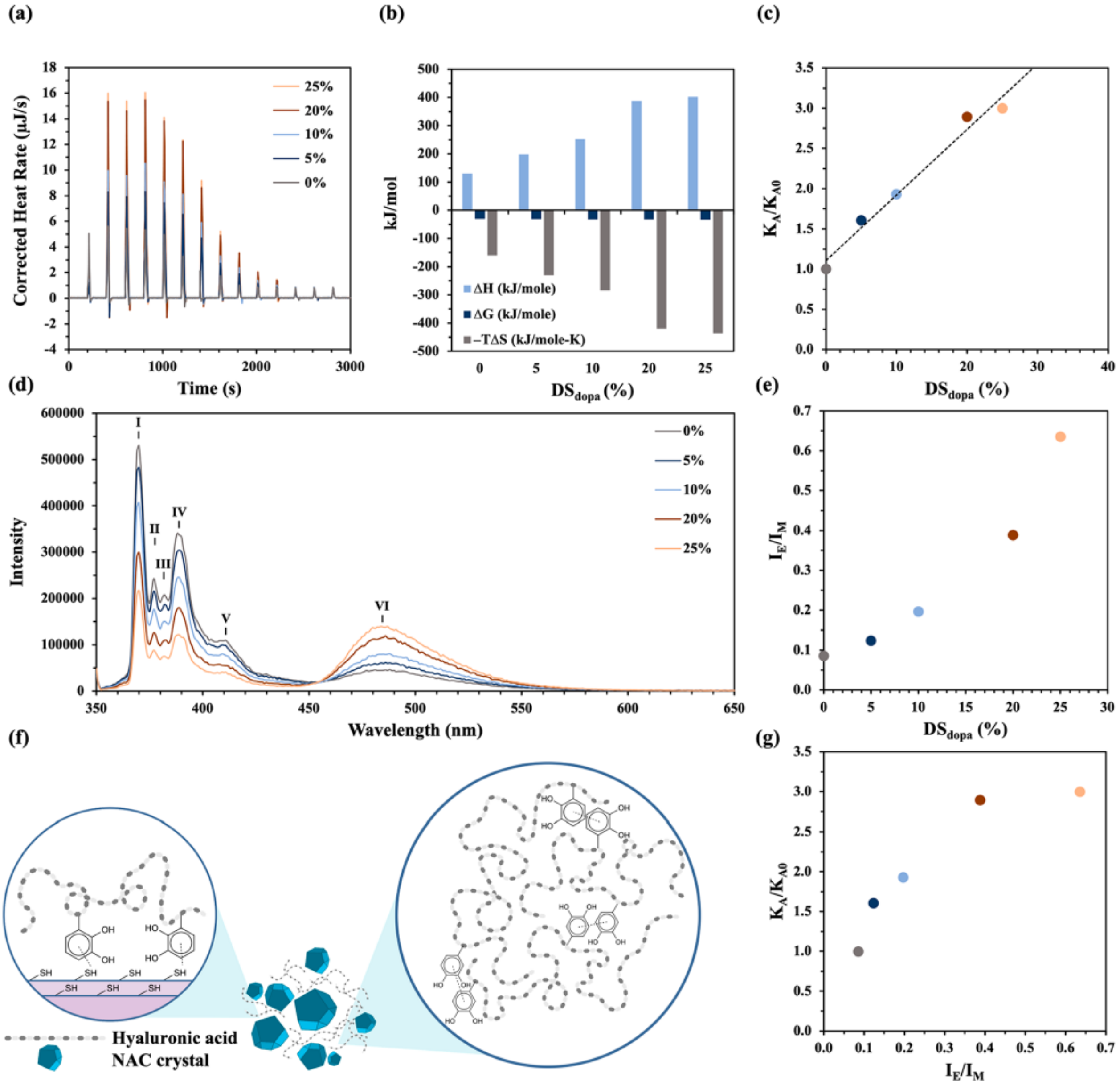

**Figure 3.** Characterization of NAC−polymer interactions and polymer−polymer interactions. (a) Corrected heat rate as a function of time for different DS$_{dopa}$. (b) Thermodynamic parameters including $\Delta G$, $\Delta H$, and $-T\Delta S$. (c) Calculated association constants normalized by the association constant for HA ($K_A/K_{A0}$). (d) Fluorescent analysis of pyrenes conjugated to different polymer formulations ranging from DS$_{dopa}$ 0 to 25%. Peaks I−V characterize the monomer peaks for pyrenes conjugated to HA-dopa, and peak VI characterizes the excimer peak for pyrenes conjugated to HA-dopa. (e) Calculated ratio between excimer ($\lambda_{Ex}$ = 485 nm) and monomer ($\lambda_{Mon}$ = 370 nm) intensities for HA conjugated with dopamine ranging from 0 to 25%. (f) Schematic illustrating drug−polymer interactions facilitated by thiol−aromatic bonds and polymer−polymer interactions facilitated by $\pi$−$\pi$ bonds. (g) NAC and polymer association constants and the ratio of excimer and monomer intensities for HA conjugated with dopamine ranging from 0 to 25%.

hydrogen bonds in the thin film. As such, the carboxylic acid monomer peak arises.

In addition to changes in the spectra at lower wavenumbers, we also observe a change above 2500 cm$^{-1}$. We used a Gauss peak function to try to deconvolute the $\nu$(C−H$_3$) and $\nu$(O−H) regions (Figure S3b,c). First, we tried fitting 7 peaks to this region, 2 each for $\nu$(C−H$_3$), 1 for $\nu$(═C−H), and 4 for $\nu$(O−H), with the assumption that there is a wide distribution of OH features. The seven-peak Gauss deconvolution succeeded for dopamine-functionalized polymers; however, the seven-peak Gauss deconvolution failed for dopamine-free HA. Subsequently, a six-peak deconvolution quickly converged for the HA spectra. We propose that this may be evidence for the $\nu$(═C−H) feature (part of the aromatic of dopamine), considering the seventh peak manifests directly in the region of ~3100 cm$^{-1}$.

### 2.2. Characterization of HA-dopamine-Stabilized NAC Crystals.

*N*-Acetylcysteine was crystallized in bulk using cooling crystallization under the following conditions: no polymer or HA-dopa with DS$_{dopa}$ ranging from 0 to 25%. The pure NAC crystals were prepared by decreasing a 10% (w/v) NAC solution temperature from 45 to 4 °C and, in turn, reducing the solubility of NAC. Separately, the polymer-stabilized NAC crystals were prepared by mixing 10% (w/v) NAC with 0.5% (w/v) HA or HA-dopa.

The major axis diameter, aspect ratio, and size distribution of the resulting crystals were characterized using scanning electron microscopy (SEM) images (Figure 2a,b). The crystallization of NAC without polymer resulted in an average major axis of 60 $\mu$m and an aspect ratio of 1.36. When NAC was crystallized in the presence of HA, the average major axis of the NAC-HA crystal was dropped to 28 $\mu$m, but the aspect ratio was not statistically different at 1.46. NAC was also crystallized with HA-dopa with different $DS_{dopa}$. The crystals made with HA-dopa (HA-dopa-stabilized NAC crystals) with a $DS_{dopa}$ of 20% showed both the smallest average major axis diameter at 13.9 $\mu$m and the narrowest particle size distribution. Like the other two conditions, the aspect ratio was not statistically different at 1.39. The decrease in crystal diameter in the presence of polymer can be explained via two mechanisms. First, the polymer functions as a nucleation site and therefore shifts the competition between nucleation events and crystal growth toward nucleation. Second, the polymer adsorbs to the surface of the growing crystal and retards crystal growth.

To explore the role of dopamine on NAC crystallization, the polymorphs of the HA-dopa-stabilized NAC crystals were characterized using powder X-ray diffraction (XRD). According to the diffraction patterns (Figure 2c), all the crystallization conditions showed the same triclinic polymorph and a high degree of crystallinity. However, while the crystal polymorph was preserved across all samples, there were notable changes in the ratios between peak intensities and peak broadening, notably peak 1 ($2\theta = 14.16$) and peak 2 ($2\theta = 15.58$), which correspond to different crystallographic planes (Figure 2d). As marked by the arrows in Figure 2d, the incorporation of dopamine in the polymer design led to substantial peak shape alterations, but the peak locations were minimally affected. As such we suspect that rather than incorporation into the crystal lattice HA-dopa preferentially adsorbs at these crystal planes. Furthermore, we observed that the ratio of peak 1 to peak 2 intensities was increased from 1.03 to 2.72 with an increase of $DS_{dopa}$ from 0 to 25%, respectively (Figure 2e).

To give a potential mechanistic explanation for the observed changes in the XRD diffractograms, we needed to better understand the intermolecular bonds present at both peak 1 and peak 2. A notable bond in NAC triclinic crystals is a N−H···S hydrogen bond that stretches along the crystallographic *b* axis.[48,49] Furthermore, peak 2 characterizes a crystallographic plane perpendicular to the crystallographic *b* axis.[48,49] We suspect that HA-dopa preferentially associates with this crystallographic plane through thiol−aromatic van der Waals forces and is a type of bond that is additive to the overall interaction between NAC and HA-dopa.

### 2.3. Thermodynamic Analysis of NAC−Polymer Interactions and Fluorescent Analysis of Polymer−Polymer Interactions.

To further explore the interaction between NAC and HA-dopa, we used isothermal titration calorimetry (ITC) to characterize the thermodynamic interaction between NAC and HA with different $DS_{dopa}$. Equimolar amounts of a 0.1 mM NAC solution were titrated into a 0.01 mM solution of either HA or HA-dopa. All conditions illustrated an endothermic association between NAC- and HA-derived polymers characterized by positive heats of adsorption (Figure 3a). Using an independent binding site model, we extracted the Gibbs free energy change of reaction ($\Delta G$), the enthalpic contribution ($\Delta H$), and the entropic contribution ($-T\Delta S$) (Figure 3b). $\Delta G$ was always negative, indicating a spontaneous event. Additionally, $\Delta G$ was independent of the $DS_{dopa}$, suggesting a minimal difference in the activation energy for the association between NAC and HA or HA-dopa.

The association between NAC and HA generated an endothermic reaction with increasing $DS_{dopa}$. Although the reaction became more endothermic with increasing $DS_{dopa}$, the presence of dopamine also increased the entropic contribution. HA is a highly hygroscopic polymer and forms strong bonds with water. Therefore, the increase in entropy can be attributed to the desolvation of HA following an interaction with NAC. Given the negative $\Delta G$ change following the endothermic reaction, we suggest that the association between the polymer and NAC was entropically driven.

The association constant ($K_A$) was also quantified to characterize how $DS_{dopa}$ influences the interaction between polymer and NAC. $K_A$ increased with $DS_{dopa}$ (Figure 3c). In particular, $K_A$ was almost 3-fold higher for HA-dopa with a $DS_{dopa}$ of 25% ($2.138 \times 10^6$ $M^{-1}$) than HA ($0.731 \times 10^6$ $M^{-1}$). This result suggests that dopamine plays a significant role in increasing the binding affinity between the polymer and drug. We propose that the initial interaction between NAC and polymer begins with desolvation and hydrogen bond formation with the HA backbone. As such, the dopamine moiety on HA-dopa further facilitates the interaction with NAC through bond formation between thiols and aromatic groups.

As observed in the ITC data, the association constants between HA-dopa with $DS_{dopa}$ of 20% and 25% are quantitatively similar. To explore if there is a value of $DS_{dopa}$ that begins to impair NAC and polymer binding, we conjugated HA with water-soluble 8-aminopyrene-1,3,6-trisulfonic acid trisodium salt (APTS). APTS molecules give different emission spectra based on their spatial position relative to other pyrenes.[50,51] These spectra can be classified as either a monomer, meaning that the emission spectra come from the excitation of nonoverlapping APTS molecules, or excimer, meaning that the emission spectra come from the excitation of overlapping APTS molecules. As such, we can use the ratio of monomer and excimer peaks in the emission spectra to elucidate the spatial arrangement of HA or HA-dopa in the solution. More intramolecular interactions between polymers would result in a higher excimer peak intensity through the aggregation of APTS, therefore providing a tool to probe how dopamine conjugation to HA influences these polymer−polymer interactions. First, we identified the monomer peak intensities with a dilute, 0.01 $\mu$M APTS solution and noted five characteristic peaks ranging from 360 to 425 nm (Figure S4a,b). Furthermore, to confirm that any excimer peak observed is a result of a pyrene−pyrene interaction, we measured the emission spectra of a free pyrene, at a fixed concentration of 0.01 $\mu$M, and unconjugated dopamine solution at several pyrene/dopamine ratios: 1:0.01, 1:0.1, 1:1, 1:10, and 1:100 (Figure S4c). We observed no changes in the emission spectra.

To study how dopamine conjugation to HA influences polymer−polymer interactions, we first conjugated APTS to HA-dopa at a number ratio of 1:100 of APTS to HA sugar residues (Figure S5). We varied the $DS_{dopa}$ from 0 to 25% to match polymer conditions studied in the ITC and XRD experiments. We note that the ratio of APTS to HA sugar residues was chosen to minimize interactions between pyrenes

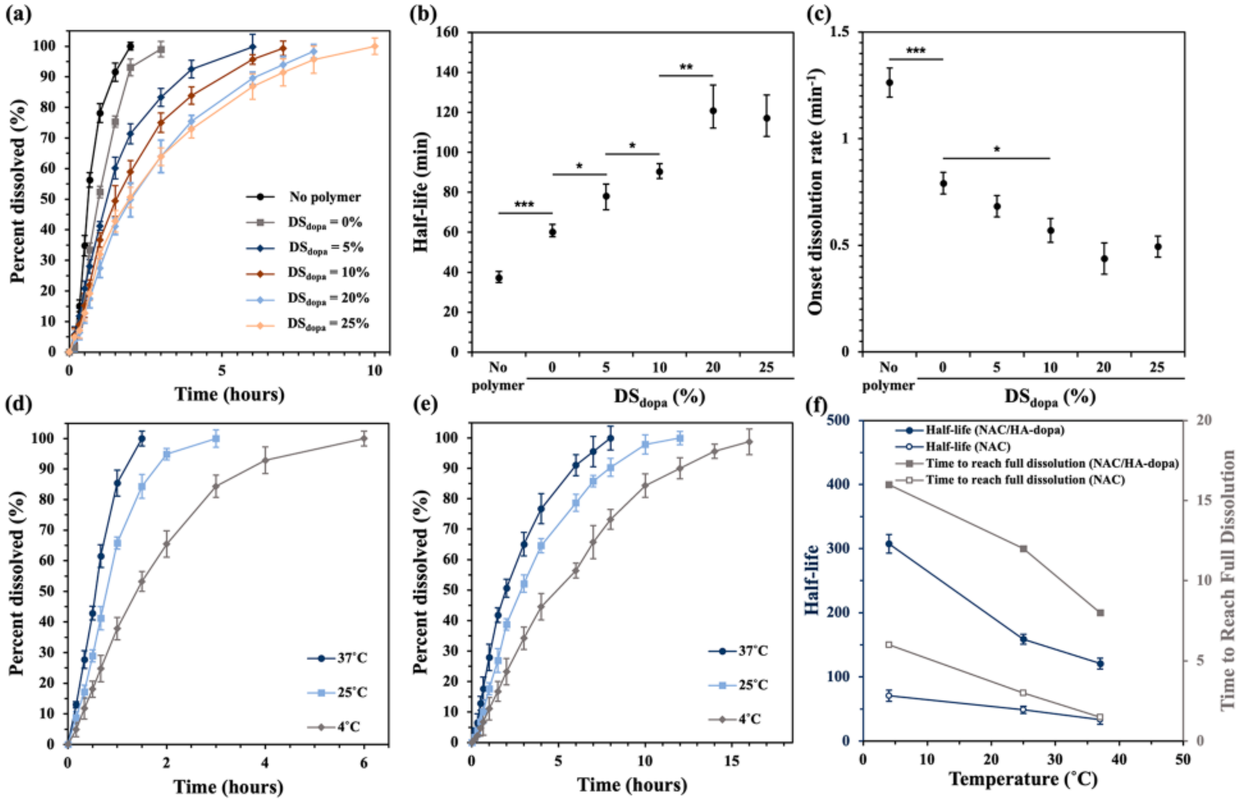

Figure 4. Analysis of NAC crystal release. (a) NAC crystal dissolution profiles in PBS at 37 °C. NAC crystals were prepared with either no polymer or HA-dopa with a controlled DSdopa. DSdopa was varied from 0 to 25%. (b) Half-life of NAC crystals. (c) Onset dissolution of NAC crystals. (d) Polymer-free NAC crystal dissolution profiles in PBS at 4, 25, and 37 °C. (e) NAC/HA-dopa (DSdopa = 20%) crystal dissolution profiles in PBS at 4, 25, and 37 °C. (f) Half-life and final dissolution time of either polymer-free NAC or NAC/HA-dopa crystals at different temperatures. In each plot, data points and error bars represent average values and 95% confidence intervals of 8 samples per condition. *, **, and *** represent the statistical significance between conditions ($*p < 0.05$, $**p < 0.01$, $***p < 0.001$) using a nonpaired $t$ test.

due to crowding. The mixing of APTS-conjugated polymers yielded a sixth peak in the emission spectra at 485 nm, which corresponds to the excimer form of APTS (Figure 3d). As such, the ratio of the excimer ($\lambda_{Ex}$ = 485 nm) and fourth monomer ($\lambda_{Mon}$ = 370 nm) peaks ($I_{Ex}/I_{Mon}$) was characterized for HA with DS$_{dopa}$ ranging from 0 to 25% (Figure 3e). We observed that probes conjugated on HA-dopa tend to aggregate more (Figure 3f), increasing the excimer/monomer emission intensity ratio ($I_{Ex}/I_{Mon}$) nonlinearly with DS$_{dopa}$. To validate that this observation is not a result of dopamine–pyrene interactions driving the rearrangement of polymers, we reduced the APTS to HA sugar residue ratio to 1:1000 and observed no statistical difference in the ratio of excimer to monomer peak intensities (Figure S6a–c). Therefore, we suggest that the $I_{Ex}/I_{Mon}$ ratio indicates that the HA–HA interaction is driven by hydrogen-bond formation, and the inclusion of dopamine increases this ratio from $\pi$–$\pi$ stacking between dopamine molecules that supplement the pre-existing hydrogen bonds. Although dopamine facilitates NAC–HA interactions, dopamine also enhances HA–HA interactions.

Finally, we plotted the relationship between $K_A/K_{A0}$ and $I_{Ex}/I_{Mon}$ (Figure 3g). We observe that increasing dopamine conjugation increases HA–HA interactions more significantly than NAC–HA interactions and note that a trade-off needs to be considered with increasing dopamine conjugation. If HA–HA interactions are too heavily favored, then crystal stability may be impaired.

**2.4. NAC Crystal Dissolution.** In order to understand the role HA and HA-dopa play in the stabilization of NAC crystals, we analyzed the dissolution behavior of NAC in PBS at 37 °C. The amount of NAC released from the crystals was measured using UV–vis spectroscopy as a function of time (Figure 4a). Polymer-free NAC crystals released NAC molecules continuously over 2 h. When crystallized in the presence of HA, the NAC crystal released NAC molecules continuously over 3 h. In contrast, NAC crystals made with HA-dopa with DS$_{dopa}$ up to 20% extended the period during which NAC molecules are released from the crystal. For instance, the NAC crystals prepared using HA-dopa with DS$_{dopa}$ of 5% continuously dissolved over 6 h, while those prepared using HA-dopa with DS$_{dopa}$ of 20% released NAC molecules over 10 h. Overall, we found that crystal fabrication with HA-dopa extended the NAC dissolution period by 3 to 5 times compared to the polymer-free NAC crystals. However, an increase of DS$_{dopa}$ above 20% did not make any significant change in the dissolution rate of NAC crystals.

We further quantified the half-life ($t_{1/2}$) and onset dissolution rate from the NAC crystal dissolution profile. The $t_{1/2}$ describes the time at which 50% of the total crystallized NAC dissolved and is a useful metric for determining dose frequencies. Figure 4b shows that the $t_{1/2}$ of polymer-free NAC crystal is 37 ± 3 min. When crystallized in the presence of HA, the $t_{1/2}$ was extended to 60 ± 4 min. In concurrence with the dissolution profiles, increasing DS$_{dopa}$ to

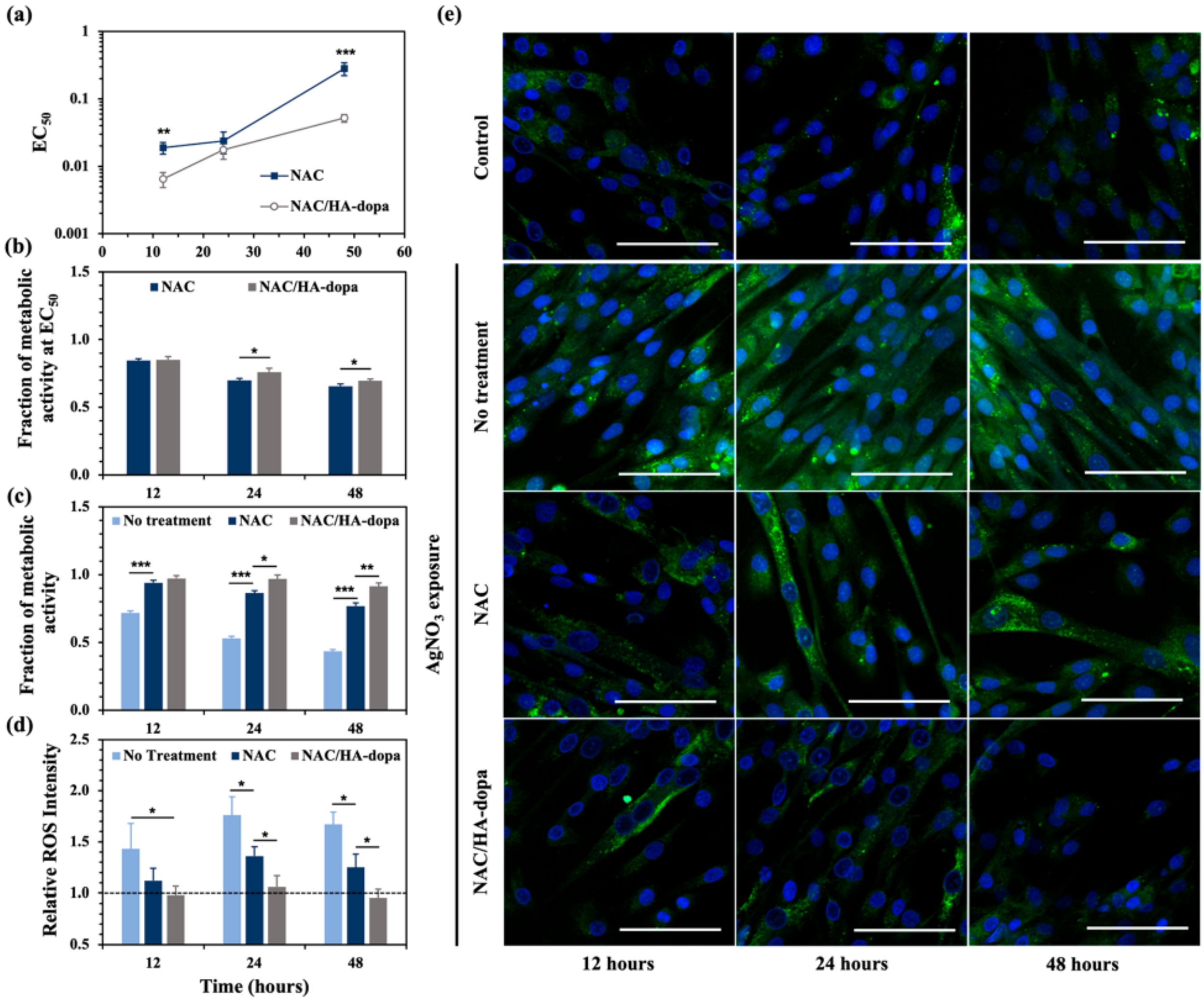

**Figure 5.** Characterization of metabolic activity and intracellular oxidative stress in differentiated H9c2 (2−1) rat cardiomyoblasts following $AgNO_3$ exposure and NAC crystal treatment. (a) $EC_{50}$ values (ppm) for NAC crystals (dark blue) and NAC/HA-dopa crystals (gray) following 0.1 ppm $AgNO_3$ exposure for 12, 24, and 48 h. (b) Fraction of metabolic activity at the $EC_{50}$ (ppm) for NAC crystals (dark blue) and NAC/HA-dopa crystals (gray). (c) Fraction of metabolic activity following 0.1 ppm $AgNO_3$ exposure for 12, 24, and 48 h and either no treatment (light blue), NAC crystal treatment (dark blue), or NAC/HA-dopa crystal treatment (gray). (d) Quantified intracellular oxidative stress in cells following 0.01 ppm $AgNO_3$ exposure for 12, 24, and 48 h and either no treatment (light blue), NAC crystal treatment (dark blue), or NAC/HA-dopa crystal treatment (gray). Dotted line represents intracellular ROS levels of a healthy population. (e) Fluorescent images of intracellular oxidative stress in cells following 0.01 ppm $AgNO_3$ exposure for 12, 24, and 48 h and either no treatment, NAC crystal treatment, or NAC/HA-dopa crystal treatment (scale bar = 100 $\mu$m). Blue stain (DAPI) represents the cell nuclei, and the green stain (CellROX Green) represents the intracellular oxidative stress. In subfigures a−d, data points and error bars represent average values and 95% confidence intervals of 5 samples per condition. *, **, and *** represent the statistical significance between conditions (*$p < 0.05$, **$p < 0.01$, ***$p < 0.001$) using a nonpaired $t$ test.

20% led to a 3-fold increase of the $t_{1/2}$ compared to the polymer-free NAC crystals.

The onset dissolution rate of the NAC crystals was obtained by linearly fitting the percentage of NAC dissolved over the first 60 min (Figure 4c). After the first 60 min, the dissolution profile began to deviate from a linear trend. The quantification of the onset dissolution provides insight into how quickly the drug begins to control the oxidative environment. Polymer-free NAC crystals had an onset dissolution of 1.3 ± 0.07%-dissolved/min. When crystallized in the presence of HA, the onset dissolution rate was decreased to 0.79 ± 0.05%-dissolved/min. As expected, the $DS_{dopa}$ for the HA-dopa-stabilized NAC crystals influenced the onset dissolution rate. In particular, NAC crystals prepared with HA-dopa with a $DS_{dopa}$ of 20% exhibited a 3-fold lower onset-dissolution rate than the polymer-free NAC crystals.

These results further validate that HA-dopa strengthens the association between NAC and HA and can be used to create NAC crystals with increased stability and prolonged NAC release. The amount of dopamine conjugated to HA was found to dictate the stability of the NAC crystals due to the coupled effect of hydrogen bonding with the polymer backbone and strong association between aromatic groups of dopamine and thiol groups of NAC, as confirmed with the ITC analysis showing the increased association with $DS_{dopa}$. Also, the intermolecular hydrogen bonding between polymers and $\pi-\pi$ stacking between dopamine molecules can lead to crystal aggregation and improved stability by forming a solvation shell with different diffusion properties based on the packing of the crystals. However, increasing $DS_{dopa}$ above 20% has a trade-off. HA-dopa with $DS_{dopa}$ of both 20% and 25% have similar NAC crystal dissolution profiles.

We further studied how temperature affects the dissolution rate of polymer-free NAC crystals and HA-dopa-stabilized NAC crystals (Figure 4d and 4e). The results show that decreasing the incubation temperature from 37 to 25 °C and 4 °C slows down the NAC crystal dissolution because of the decreased NAC solubility at lower temperatures. Accordingly, the half-life and time to reach full dissolution increased with decreasing incubation temperature (Figure 4f). The dependency of the half-life and time to reach full dissolution on the temperature was larger for HA-dopa-stabilized NAC crystals.

**2.5. Efficacy of NAC/HA-dopa Crystals to Protect Rat Cardiac Muscle Sheets Exposed to $AgNO_3$.** The antioxidant activity of the NAC crystals over 48 h was tested by examining both the metabolic activity and intracellular oxidative stress in rat cardiomyotubes following silver nitrate ($AgNO_3$) exposure. As previously reported, silver ions are a major toxic component of AgNPs and drive AgNP cytotoxicity through ROS production. As such, we used $AgNO_3$ to produce silver ions that could be taken up by the cells and promote oxidative stress. We first characterized the half-maximal effective concentration ($EC_{50}$) of $AgNO_3$ following 24 h of exposure, to establish a condition in which there was a significant reduction in cell metabolic activity observed over a 48 h exposure and treatment condition (Figure S7a,b). We found that following a 24 h exposure time to 0.1 ppm $AgNO_3$, only 53.2% of the original metabolic function was retained. For the remainder of the metabolic characterization, the $AgNO_3$ exposure concentration was fixed, but the treatment conditions were varied.

To illustrate the improved efficacy of HA-dopa-stabilized NAC crystals, rat cardiac muscle sheets were exposed to $AgNO_3$ and subsequently treated with either a polymer-free NAC crystal suspension or a NAC/HA-dopa ($DS_{dopa}$ = 20%) crystal suspension for 12, 24, and 48 h. In the first study, we varied the concentration of each crystal formulation (Figure S8a−c) and compared the $EC_{50}$ values, defined as the $AgNO_3$ concentration resulting in 50% reduction in metabolic activity (Figure 5a). At both the 12 and 48 h time points, the $EC_{50}$ of the polymer-free NAC crystal was higher than that of the HA-dopa-stabilized NAC crystal, illustrating the larger NAC dose requirement to preserve 50% of the maximum metabolic function. We note that there will be irreversible cellular damage since the NAC treatment was 30 min post $AgNO_3$ exposure. The metabolic function for both crystal systems approaches a maximum value below that of a healthy population. We further point out that after 12 h there is a statistical difference in the maximum metabolic function for both crystal systems, resulting in $EC_{50}$ values corresponding to different metabolic activities. We also report the metabolic activity following treatment of both crystal systems at their respective $EC_{50}$ values (Figure 5b). At 24 and 48 h post-treatment, the HA-dopa-stabilized NAC crystal preserved a higher degree of metabolic function in the cardiac muscle sheets than the polymer-free NAC crystal.

The Hill coefficient ($c_H$), the slope at the inflection point, is another valuable metric for comparing the efficacy of the crystal systems (Figure S8d). A larger $c_H$ indicates that the effective concentration range to preserve metabolic activity is narrower and would suggest the requirement of a more frequent dosing regimen. Our study shows that: (1) The $c_H$ increases as a function of exposure time for the HA-free NAC crystal system. In contrast, there is no statistical difference in $c_H$ for the HA-dopa-stabilized crystal. This result demonstrates that the increased working time of the NAC crystals aligns well with the prolonged release of NAC. (2) Furthermore, the $c_H$ is higher for the polymer-free NAC crystal system than for the HA-dopa-stabilized NAC crystal system at 24 and 48 h.

In addition to $EC_{50}$ characterization for both crystal systems, we compared the maintenance of metabolic activity at a fixed NAC crystal dose. Cardiac muscle sheets were first exposed to 0.1 ppm $AgNO_3$ and treated with either a 5 ppm polymer-free NAC crystal suspension or a 5 ppm NAC/HA-dopa ($DS_{dopa}$ = 20%) crystal suspension for 12, 24, and 48 h (Figure 5c). The NAC concentration of 5 ppm was chosen based on no observed decrease in metabolic function at this concentration (Figure S7d). Furthermore, we tested if HA-dopa may elicit a toxic response by probing the metabolic state of the cells (Figure S7e). Even at a concentration 100 times larger than we used in our treatment studies, there was no statistical difference in the metabolic function of the cells compared to the no-treatment control. Following $AgNO_3$ exposure, there was a significant decrease in metabolic activity for the no-treatment group. The fraction of metabolic activity decreased to as low as 0.39 ± 0.05 over 48 h of exposure. NAC crystal treatment post $AgNO_3$ exposure served to preserve metabolic function. The duration of antioxidant activity depended on the NAC crystal stability and release. In particular, after 12 h, both polymer-free NAC and HA-dopa-stabilized NAC crystals maintained over 90% of the original metabolic activity.

However, the efficacy difference between the two NAC crystal systems became significant over the next 36 h. The fraction of metabolic activity decreased by 24% when treated with polymer-free NAC crystals. In contrast, the HA-dopa-stabilized NAC crystals effectively retained metabolic activity at 90%. The extended duration of preserved metabolic function in the muscle sheets is attributed to the more sustained release of NAC from the HA-dopa-stabilized NAC crystals, as characterized by the dissolution profile shown in Figure 4. To confirm that the efficacy of the crystals is a result of the release of NAC and not the polymer, we conducted additional MTT studies with only HA-dopa. We did not see any direct effects on the metabolic activity (Figure S7f).

Since we propose that the drug efficacy comes from the antioxidant behavior, we quantified the intracellular oxidative stress in rat cardiac muscle sheets exposed to 0.01 ppm $AgNO_3$ and related these levels to the ROS-scavenging potential of the NAC crystals. Since we observed cell death from the $AgNO_3$ $EC_{50}$, we used the effective concentration at 20% of the maximal value ($EC_{20}$) (Figure S7c) for this experiment, as to only put cells into an acute state of oxidative stress. In order to quantify the intracellular ROS levels, we used a fluorescent probe, CellROX Green. In the reduced state, the cell-permeant dye is weakly fluorescent; however, it emits a green, fluorescent signal at 520 nm upon oxidation by intracellular ROS. The corrected total cell fluorescence was collected at 12, 24, and 48 h (Figure 5d), where the cell fluorescence value represents the intracellular oxidative stress level. The corrected fluorescent values were normalized to the fluorescent value of healthy cells that were not exposed to $AgNO_3$.

Cells exposed to $AgNO_3$ showed an increase in the intracellular oxidative stress up to 48 h, as marked by the increased fluorescence intensity (Figure 5e). In agreement with previous mechanistic studies, increased ROS levels are likely a result of increased intracellular ROS production, prolonged survival through the deactivation of endogenous antioxidant pathways, or a combination of both.[5,9−12] Interestingly, at each

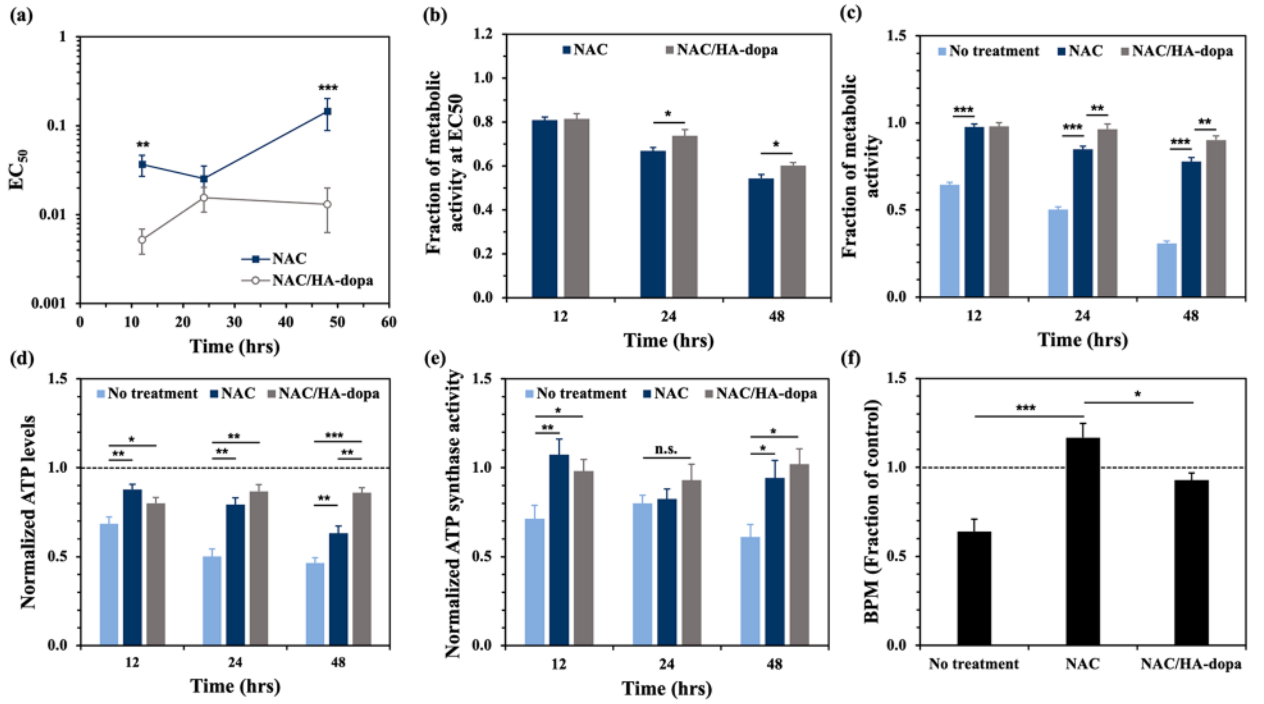

**Figure 6.** Characterization of metabolic activity, ATP, ATP synthase, and contraction frequency in iCell human cardiomyocytes following $AgNO_3$ exposure and NAC crystal treatment. (a) $EC_{50}$ values (ppm) for NAC crystals (dark blue) and NAC/HA-dopa crystals (gray) following 0.1 ppm $AgNO_3$ exposure for 12, 24, and 48 h. (b) Fraction of metabolic activity at the $EC_{50}$ (ppm) for NAC crystals (dark blue) and NAC/HA-dopa crystals (gray). (c) Fraction of metabolic activity following 0.1 ppm $AgNO_3$ exposure for 12, 24, and 48 h and either no treatment (light blue), NAC crystal treatment (dark blue), or NAC/HA-dopa crystal treatment (gray). (d) Quantified ATP levels following 0.01 ppm $AgNO_3$ exposure for 12, 24, and 48 h and either no treatment (light blue), NAC crystal treatment (dark blue), or NAC/HA-dopa crystal treatment (gray). Dotted line represents intracellular ROS levels of healthy population. (e) Quantified ATP synthase activity following 0.01 ppm $AgNO_3$ exposure for 12, 24, and 48 h and either no treatment (light blue), NAC crystal treatment (dark blue), or NAC/HA-dopa crystal treatment (gray). (f) Contractions per minute following 0.01 ppm $AgNO_3$ exposure for 48 h and either no treatment, NAC crystal treatment, or NAC/HA-dopa crystal treatment. Dotted line represents intracellular ROS levels of a healthy population. In subfigures a−f, data points and error bars represent average values and 95% confidence intervals of 5 samples per condition. *, **, and *** represent the statistical significance between conditions ($*p < 0.05$, $**p < 0.01$, $***p < 0.001$) using a nonpaired $t$ test.

time point, HA-dopa-stabilized NAC crystals showed both lower intracellular ROS levels compared to the no-treatment group and no statistical significance from the control (represented as a normalized ROS intensity of 1.0). Polymer-free NAC crystals also decreased the intracellular oxidative stress compared to untreated cells, but intracellular ROS levels were still elevated compared to the healthy cell population.

**2.6. Efficacy of NAC/HA-dopa Crystals to Protect Human Cardiomyocytes Exposed to $AgNO_3$.** To extend the observed efficacy trends in rat cardiomyotubes to human cells, we utilized an induced pluripotent stem cell (iPSC)-derived human cardiomyocyte model. This model displays characteristic synchronous beating that can be used to simulate tissue function post $AgNO_3$ exposure and NAC crystal treatment. In accordance with the rat cardiac muscle sheet study, we characterized the metabolic activity in two ways: (1) direct comparison of the $EC_{50}$ values for polymer-free NAC crystals and HA-dopa-stabilized NAC crystals and (2) comparison at fixed NAC crystal concentrations. We further characterized both the cellular ATP levels and ATP synthase activity.

In the first study, we varied the concentration of each crystal formulation (Figure S9a−c) and compared the $EC_{50}$ values (Figure 6a). At both the 12 and 48 h time points, the $EC_{50}$ of the polymer-free NAC crystals was higher than that of the HA-dopa-stabilized NAC crystals, illustrating a larger dose requirement to preserve 50% of the maximum metabolic function. For the metabolic activity of both crystal systems at their respective $EC_{50}$ values (Figure 6b), the HA-dopa-stabilized NAC crystal system preserves a higher degree of metabolic function in the $AgNO_3$-exposed cardiac muscle sheets than the polymer-free NAC crystal system at 24 and 48 h. Like before, we characterized the $c_{\mathrm{H}}$ (Figure S9d) and observed an increase as a function of exposure time for the polymer-free NAC crystal system. In contrast, the HA-dopa-stabilized system did not show a statically significant change. Additionally, the $c_{\mathrm{H}}$ was higher for the polymer-free NAC crystal system than the HA-dopa-stabilized NAC crystal system at 24 and 48 h.

In addition to $EC_{50}$ characterization for both crystal systems, we compared the maintenance of metabolic activity at fixed NAC crystal suspension concentrations. Again, the cardiac muscle sheets were first exposed to 0.1 ppm $AgNO_3$ and treated with either a 5 ppm polymer-free NAC crystal suspension or a 5 ppm NAC/HA-dopa ($\mathrm{DS}_{\mathrm{dopa}} = 20\%$) crystal suspension for 12, 24, and 48 h (Figure 6c). Following $AgNO_3$ exposure, there was a significant decrease in metabolic activity for the no-treatment group. The fraction of metabolic activity decreased to as low as 0.31 ± 0.03 within 48 h of exposure. NAC crystal treatment post $AgNO_3$ exposure served to preserve metabolic function. Again, we observed that the

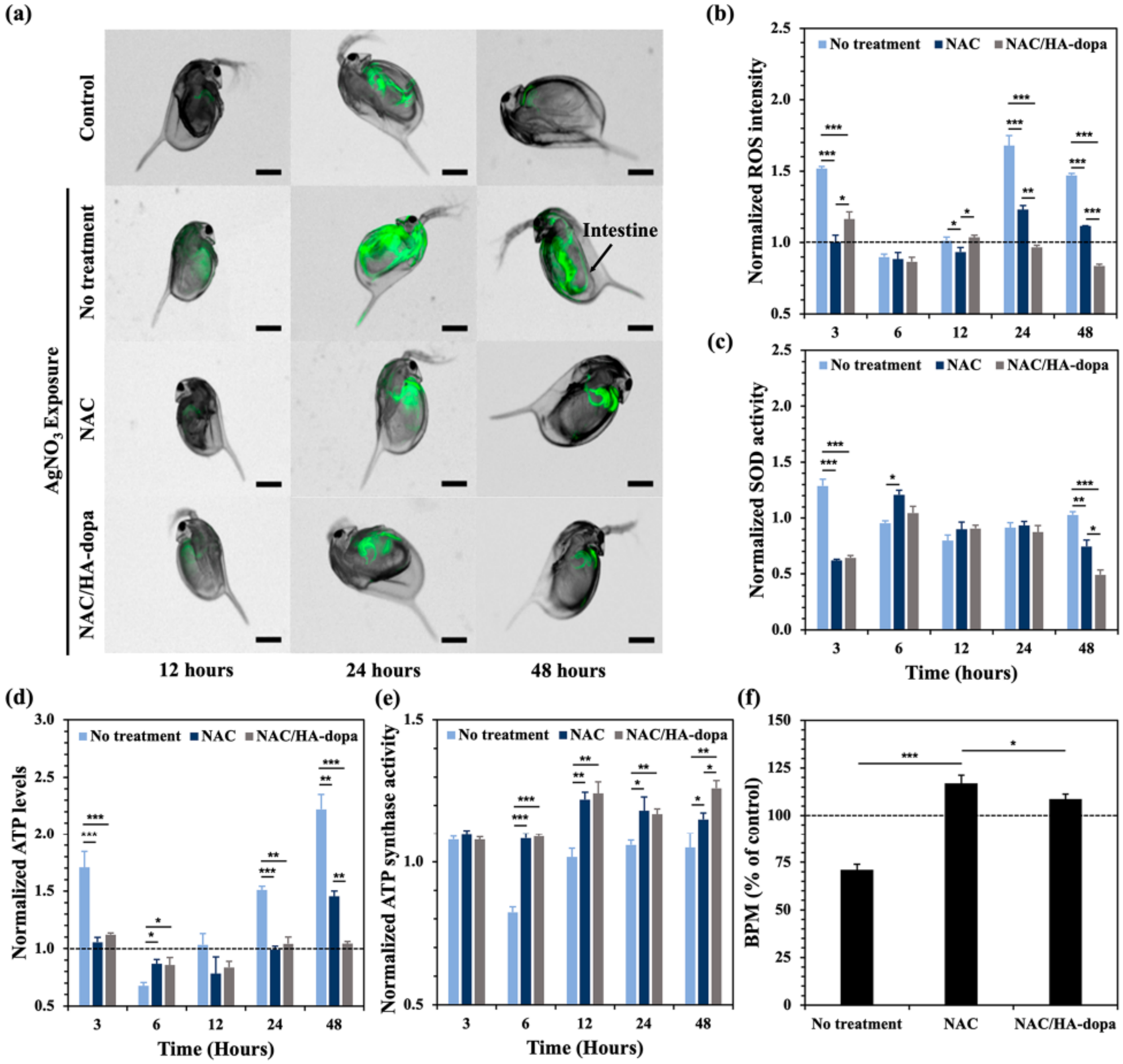

Figure 7. Protective effects of NAC crystals against $AgNO_3$-induced oxidative stress in the *Daphnia magna* model. Daphnids were exposed to 0.001 ppm $AgNO_3$ for up to 48 h. (a) Fluorescent images depicting oxidative stress in *Daphnia magna* (scale bar = 300 $\mu$m). (b) ROS intensity normalized to a population that was not exposed to $AgNO_3$. Dotted line represents intracellular ROS levels of a healthy population. (c) SOD intensity levels normalized to a population that was not exposed to $AgNO_3$. (d) ATP intensity levels normalized to a population that was not exposed to $AgNO_3$. Dotted line represents intracellular ROS levels of a healthy population. (e) ATP synthase activity levels normalized to a population that was not exposed to $AgNO_3$. (f) Heart rate (BPM) at 48 h normalized to a population that was not exposed to $AgNO_3$. Dotted line represents intracellular ROS levels of a healthy population. Data points and error bars represent average values and 95% confidence intervals of 20 samples per condition. *, **, and *** represent the statistical significance between conditions (*$p < 0.05$, **$p < 0.01$, and ***$p < 0.001$) using a nonpaired $t$ test.

antioxidant activity duration depended on the NAC crystal stability and release. In particular, after 12 h, both polymer-free NAC and HA-dopa-stabilized NAC crystals maintained over 90% of the original metabolic activity. However, the efficacy difference between the two different NAC crystal systems became significant over the next 36 h. The fraction of metabolic activity decreased by 22% when treated with polymer-free NAC crystals. In contrast, the HA-dopa-stabilized NAC crystals were effective in retaining metabolic activity at 90%.

To further explore the metabolic function of the human cardiomyocytes post silver ion exposure, we quantified both the cellular ATP levels and the ATP synthase activity levels (Figure 6d,e). In accordance with our previous methods, we used the $AgNO_3$ $EC_{20}$ value to evaluate the effects of acute oxidative stress and monitor deviations in the intracellular function. Following 0.01 ppm $AgNO_3$ exposure to the human cardiac muscle sheets, ATP levels and ATP synthase activity significantly deviated from the levels in cardiac muscle sheets that were not exposed to silver ions. The deviation was the most extreme at 48 h. ATP levels deviated by 63%, and ATP synthase activity levels deviated by 39%. Abnormal changes in ATP levels and ATP synthase levels were mitigated by NAC crystal treatment. In particular, at 48 h, the HA-dopa-stabilized NAC crystals minimized the ATP level deviation across all treatment groups.

One major advantage of the iCell cardiomyocyte cell line is that they synchronously contract spontaneously when confluent. To illustrate that the antioxidant crystals can preserve normal tissue function post silver ion exposure, the number of contractions per minute was quantified for either no-treatment, polymer-free NAC crystal treatment, or HA-dopa-stabilized NAC crystal treatment (Figure 6d–f). Interestingly, we saw a suppression in contraction frequency for the no-treatment group and increased contraction frequency for the polymer-free NAC crystal treatment group. The HA-dopa-stabilized NAC crystal treatment group was not statistically different from the human cardiomyocytes not exposed to $AgNO_3$. This nicely illustrates the need for balanced intracellular ROS levels for normal tissue function by demonstrating that unregulated oxidative stress can result in abnormal beating behavior in human cardiac muscle sheets.

**2.7. *In Vivo* Analysis of the Extent That NAC/HA-dopa Crystals Protect *Daphnia magna* Exposed to $AgNO_3$.** In addition to potential toxic effects in humans, silver ions released in aquatic ecosystems can have drastic implications on the health of microorganisms such as the freshwater zooplankton *Daphnia magna*.[46−48] As such, this species is extensively used to assess nanoparticle toxicity due to its sensitivity (Figure S10b) and filter-feeding behavior that aids in the oral uptake of nanoparticles or freshwater contaminants.[46] In this study, young daphnids were exposed to media supplemented with 0.001 ppm $AgNO_3$ (determined as the $EC_{20}$ from Figure S10a) and either treated with 5 ppm polymer-free NAC crystals or 5 ppm HA-dopa-stabilized NAC crystals. As previously noted, silver ions induce intracellular oxidative stress and influence the endogenous antioxidant system of cells. In agreement with the rat cardiac muscle study, we assessed the ROS levels but further characterized the endogenous antioxidant system through the characterization of the enzyme, superoxide dismutase (SOD) (Figure 7a–c). Both ROS and SOD levels were monitored over 48 h.

Initially, the ROS levels for the no-treatment and HA-dopa-stabilized NAC administration conditions showed an increase in ROS level, but at 6 h all conditions had quenched overproduced ROS. Nonetheless, after 6 h the ROS levels continued to increase and at 48 h were over 2-fold higher than the control conditions. The increase in ROS levels followed by no recovery suggests that by 6 h the endogenous antioxidant system has become overwhelmed following $AgNO_3$ exposure and no exogenous antioxidant treatment. When comparing the polymer-free and the HA-dopa-stabilized NAC crystal systems, the polymer-free NAC crystals showed better ROS control in the first 12 h. This result aligns well with the dissolution study and highlights that fast release leads to improved oxidative stress control in the short term. However, at 24 h, control over the oxidative environment has been lost. In contrast, at 24 and 48 h there was no increase in intracellular ROS following treatment with HA-dopa-stabilized NAC crystals. While the polymer-free NAC crystals display therapeutic potential, the colloidal crystals highlight their ability for prolonged redox control. Moreover, delivery of both antioxidant systems showed reduced ROS levels in the intestine, the expected residence site of the NAC crystals, and around the heart (Figure 7a). Increased ROS levels near and in the heart were observed for the no-treatment condition, especially at 24 h. This result indicates that both NAC crystal systems are able to control the oxidative environment initially at the local site of delivery. However, only the HA-dopa-stabilized NAC crystals could offer oxidative protection to the surrounding tissue sustainably.

SOD is an endogenous antioxidant system found in the *Daphnia magna*. At 3 h postexposure to $AgNO_3$ and no NAC treatment, there was an increase in SOD level. This result indicates that the intracellular ROS generation resulting from $AgNO_3$ exposure promotes SOD activity as an endogenous response to oxidative stress. In contrast, NAC crystal delivery showed initial suppression of SOD activity, and at 48 h the HA-dopa-stabilized NAC crystals led to significant suppression of SOD activity compared to the polymer-free NAC crystals. Coupled with the ROS measurement, this result suggests that the extended release of NAC from HA-dopa-stabilized crystals serves to suppress the SOD activity by scavenging ROS generation.

In addition to measuring ROS levels and SOD activity levels, the ATP levels were measured over 48 h (Figure 7d). $AgNO_3$ exposure followed by no NAC treatment caused two observable spikes in ATP levels. The first occurred at 3 h. Then, the ATP level decreased back to normal at 6 h. This is likely because of the activation of the endogenous antioxidant system to control ROS levels. After 6 h, however, the ATP levels continuously increased, suggesting the endogenous antioxidant system became overwhelmed. In contrast, daphnids treated with both NAC crystal formulations showed no increase in ATP levels during the first 12 h. After 24 h, the daphnids treated with the polymer-free NAC crystals showed a moderate increase in the ATP level, although the degree of increase was smaller than the no-treatment condition. Interestingly, the daphnids treated with HA-dopa-stabilized NAC crystals exhibited a minimal increase in the ATP level, which is well aligned with the observed sustained release of NAC molecules from the crystals.

We further analyzed the changes in the ATP synthase activity (Figure 7e). The no-treatment condition showed minimal upregulation in ATP synthase activity. The observed elevation in ATP levels for the no-treatment condition, as previously discussed, is therefore not a result of increased ATP production and, instead, an indicator that ATP is not being consumed. We theorize that ATP levels do not diminish because of an impaired pathway to ATP hydrolysis propagated by elevated ROS production seen at the same time points. In contrast, daphnids treated with NAC crystals, particularly HA-dopa-stabilized NAC crystals, showed continuously higher ATP synthase levels than the no-treatment condition. ATP synthase levels were likely to increase due to cellular damage caused by silver ions. Although ATP synthase levels increased, we did not see an increase in ATP levels which may be an indicator that increased ATP hydrolysis is a natural response to healing. We propose that NAC molecules sustainably released from the crystals enter cells and lead to endogenous glutathione production and maintenance of ROS homeostasis. In turn, it is likely that individual cells in daphnids are active to produce and hydrolyze ATP at a healthy level.

To further highlight the cardioprotective effects of NAC crystals, the heart rate of the daphnids post 48 h $AgNO_3$ exposure and treatment was quantified (Figure 7f). The translucent body of the daphnids make monitoring the heart rate feasible (Movies S5–S8), and the heart rate was characterized as beats per minute (BPM) using a high-speed camera. No treatment following $AgNO_3$ exposure led to over a 25% reduction in the heart rate. In contrast, the polymer-free NAC crystals resulted in a small increase in heart rate, while the HA-dopa-stabilized crystals showed no statistical difference from the normal heart. The preservation of the daphnid heart rate by the HA-dopa-stabilized NAC crystals further highlights their therapeutic efficacy, resulting from a prolonged release profile.

## 3. CONCLUSION

This study demonstrated a new hydrophilic antioxidant delivery system that was proper to achieve prolonged ROS homeostasis in the context of silver-ion exposure. We found that NAC could be crystallized and stabilized with HA-dopamine through (1) coupled entropically driven hydrogen-bond formation and dopamine−thiol interactions and (2) aggregation due to $\pi-\pi$ stacking between dopamine molecules and hydrogen bonds between HA. The resulting HA-dopa-stabilized NAC crystal released NAC molecules continuously over 10 h, while the polymer-free NAC crystals dissolved within 2 h. Thus, HA-dopa-stabilized NAC crystals could protect cardiac muscle sheets and *Daphnia magna* over 48 h after exposure to sublethal dosing of $AgNO_3$. According to the biochemical analysis, the HA-dopa-stabilized NAC crystals retain ROS and endogenous antioxidizing activities at normal levels. The improved antioxidizing activity of the HA-dopa-stabilized NAC crystal is attributed to the sustained NAC release. As such, the NAC molecules would scavenge exogenous ROS and, also, stimulate cellular antioxidant synthesis. We proposed that this antioxidant crystal platform can be used to treat cardiac exposure to toxic metallic ions through either intramuscular or intravascular delivery; however, the administration route could be modified based on the target tissue. Furthermore, metal-ion exposure in aquatic systems can be mediated by the oral uptake of the crystal system by essential microorganisms such as *Daphnia magna*. Finally, we envision HA-dopa would be used to improve the efficacy of a wide range of active pharmaceutical ingredients through enhanced crystal stability.

## 4. EXPERIMENTAL SECTION

**4.1. Materials.** *N*-Acetyl-L-cysteine (NAC) (>99%), *N*-(3-(dimethylamino)propyl)-*N′*-ethylcarbodiimide hydrochloride (EDC) (98%), *N*-hydroxysulfosuccinimide sodium salt (sulfo-NHS) (>98%), 4-morpholineethanesulfonic acid monohydrate (MES) (>99%), dopamine hydrochloride, 8-aminopyrene-1,3,6-trisulfonic acid trisodium salt (APTS), and silver nitrate (>99%) were purchased from Sigma-Aldrich. Hyaluronic acid (HA, Mw ≈ 620−1200 kg/mol) was purchased from Kikkoman. For polymer purification and drug release tests, a dialysis tube (MWCO: 500−1000 Da, Spectrum Laboratories) was used. H9c2(2−1) cells (rat myoblast cell line from myocardium) were obtained from American Type Cell Culture (ATCC CRL-1446) and cultured according to the guidelines of ATCC. iCell human cardiomyocytes (human iPSC-derived) were obtained from FUJIFILM Cellular Dynamics, Inc. (FUJI 11713) and cultured according to the supplier's guidelines. Daphnia eggs were obtained from Environmental Bio-Detection Products Incorporation (EBPI, Daphtoxkit F magna) and cultured according to the standard operational procedure.

**4.2. Synthesis of HA Conjugated with Dopamine (HA-dopa).** The degree of substitution of dopamine ($DS_{dopa}$) was controlled by changing the molar ratio between dopamine and sodium glucuronate of HA from 2:9 to 4:9, 8:9, and 10:9. HA was dissolved in a 0.1 M solution of MES (pH = 5) for 12 h at room temperature. Once the polymer was fully dissolved, 1-ethyl-3-(3-(dimethylamino)propyl) carbodiimide (EDC) and *N*-hydroxysulfosuccinimide (sulfo-NHS) were dissolved in the solution for 30 min. EDC and sulfo-NHS were both added in excess at a 0.625:1 molar ratio to sodium glucuronate of HA. Dopamine hydrochloride was added at the appropriate molar ratio. The mixture was dialyzed against DI water using a dialysis tube (MWCO = 3.5 kDa) for 2 days and then lyophilized for 3 days before storage at 4 °C until future use.

**4.3. Characterization of Dopamine Conjugation to HA.** $^1H$ NMR (600 MHz, $D_2O$) was run for dopamine, HA, and H-dopa. Each scan was run at 25 °C in $D_2O$, and MestReNova software was used for characterization. Infrared spectra of HA-dopa provide spectroscopic evidence of polymer functionalization with dopamine. Polymers were drop cast (in aqueous solution) as a thin film on $CaF_2$ windows at 65 °C and dried under vacuum for 12 h to remove residual water before being sealed within a custom-built, temperature-controlled transmission cell attached to a gas-handling manifold under He flow (10 cm−3 $min^{-1}$; Airgas, Ultrazero grade) mounted inside an FTIR spectrometer (Bruker, Vertex 70) coupled with a liquid $N_2$-cooled HgCdTe detector. Spectra were obtained at 313 K (128 scans, 4 $cm^{-1}$ resolution) after background spectra were obtained under identical conditions with an empty transmission cell containing no polymer.

**4.4. Preparation of NAC Crystals by Polymer-Directed Crystallization.** An amount of 50 mg (5% w/w of NAC) of polymer additives (hyaluronic acid or hyaluronic acid conjugated with dopamine) was dissolved in DI water (10 mL) for 6 h at 45 °C to ensure the complete dissolution. Then, 1g of NAC was added into the polymer solution and stirred at 45°C until all the solids were dissolved (6 h). The mixture was cooled to 4 °C at a controlled rate of 1 °C/min, and the crystallization was allowed to proceed for 24 h. The obtained crystal solution was filtered through a poly(vinylidene fluoride) (PVDF) membrane (HVLP04700, pore size: 0.45 μm, Millipore) to collect NAC crystals. The crystals were gently washed 2−3 times with DI water to remove the unbound polymers. Then, the samples were dried under vacuum at room temperature for 2 days. NAC crystals were stored at room temperature under $N_2$ until used for future experiments.

**4.5. NAC Crystal Characterization.** The morphology of NAC crystals was examined by an optical microscope (Leica DMIL) and an environmental scanning electron microscope (ESEM, Quanta FEG 450, FEI) at 7 kV acceleration voltage. Fifty crystals from five ($n = 5$) different SEM images of each population were analyzed to measure the average crystal size and aspect ratio, as determined with ImageJ. Powder X-ray diffraction (MiniFlex 600, Rigaku) was conducted to observe changes in the contents of crystal phases. The scans were performed in the 2-theta range of 10−70 at 5°/min.

**4.6. Thermodynamic Analysis of NAC−Polymer Interactions.** Thermodynamic analysis of the association between NAC and polymer additives was performed by isothermal titration calorimetry (TA AffinityITC). The 300 μL sample cell was filled with a 0.01 mM polymer solution. The cell was titrated with 28 injections of 5 μL NAC solution (0.1 mM). Each injection was performed over 18 s with a delay of 250 s between injections while stirring at 300 rpm. Thermodynamic binding parameters such as the binding constant, the change in enthalpy, and the change in entropy were obtained and calculated by fitting data to a single-site binding model. The first data point was not included in the analysis.

**4.7. Fluorescent Analysis of the Self-Organization between HA Polymers.** APTS was dissolved in a HA-dopa solution and conjugated via the same carbodiimide chemistry described above, resulting in a 1:100 ratio of APTS to sugar monomer of HA. The conjugation of APTS to HA and HA-dopa was confirmed with a standard curve quantifying the summation of the monomer ($\lambda_{Mon}$ = 370 nm) and excimer ($\lambda_{Ex}$ = 485 nm) peak intensities. The resulting pyrene-conjugated polymer was loaded into a quartz cuvette at a concentration of 0.01 μM and excited at a wavelength of 343 nm. The emission spectra were recorded from 350 to 650 nm for HA-dopa with $DS_{dopa}$ ranging from 0% to 5%, 10%, 20%, and 25% with a fluorometer (Fluoromax-4, Jobin Yvon).

**4.8. Analysis of the Dissolution Profile of NAC Crystals.** An amount of 50 mg of NAC crystals was placed in a dialysis tube (MWCO = 500−1000 Da) with phosphate-buffered saline (PBS, 1 mL). The dialysis tube was placed in 499 mL of PBS media and incubated at either 37 °C, 25 °C, or 4 °C under continuous shaking at 100 rpm. At the designated time points, dissolved NAC was collected from the incubation media and determined by reading the absorbance at the wavelength of 260 nm using the microplate spectrophotometer (Infinite 200 PRO, Tecan).

**4.9. *In Vitro* Testing.** *4.9.1. Analysis of the Metabolic Activity of H9c2(2−1) Cells and iCell Human Cardiomyocytes.* A commercially available MTT assay kit (11465007001, Roche) was used to measure the metabolic activity of cells exposed to $AgNO_3$. The assay was performed with several modifications to the manufacturer's directions. H9c2(2−1) cells were seeded onto 96-well plates at a density of 10 000 cells per well. When the cells reached 80% confluency, the FBS in the cell media was reduced from 10% to 1%. By doing so, the myoblasts fused and differentiated into myotubes. After differentiation, the cells reached full confluency and formed a monolayer cell sheet. iCell human cardiomyocytes were seeded onto 96-well plates at a density of 40 000. After 2 days the medium was switched from the supplier's plating media to the supplier's maintenance media. Both cell lines were further incubated with either 0 ppm $AgNO_3$ as the control or 0.1 ppm $AgNO_3$ as the sublethal conditions for 12, 24, or 48 h. During the $AgNO_3$ exposure, cells were supplemented with either no NAC, 5 ppm of NAC, or 5 ppm of NAC/HA-dopa ($DS_{dopa}$ = 20%). After that, 90 μL of growth media (0.1% FBS) and 10 μL of MTT solution were then added to each well. The cells were incubated for 3 h at 37 °C. The formazan crystals formed in each well were solubilized using 65 μL of DMSO upon removal of growth media. The absorbance of MTT was measured by using a microplate spectrophotometer (Infinite 200 PRO, Tecan) at the wavelength of 550 and 650 nm. The relative metabolic activity of cells was quantified as [(A550−A650) sample/(A550−A650) control]. Five samples ($n$ = 5) were prepared for each condition.

*4.9.2. Analysis of the Intracellular Oxidative Stress in H9c2(2−1) Cells.* H9c2(2−1) cells were seeded on poly-D-lysine coated 18 mm cover glass at 10 000 cells/dish and differentiated as described before. After differentiation, cells were exposed to either 0 ppm $AgNO_3$ as the control or 0.01 ppm $AgNO_3$ as the sublethal condition along with either no NAC, 5 ppm of NAC, or 5 ppm of NAC/HA-dopa ($DS_{dopa}$ = 20%). After 12, 24, or 48 h, the intracellular oxidative stress was evaluated using the cellROX green reagent (ThermoFisher), following the manufacturer's instruction. Briefly, the H9c2(2−1) cells were incubated with 5 μM cell ROX reagent for 30 min, and the cells were washed with 1X PBS three times. The cells were fixed with a 1:1 acetone/methanol solution for 15 min. For the nuclear counterstain, cells were stained with 500 nM 4′,6-diamidino-2-phenylindole (DAPI). Finally, the cells were imaged using a confocal microscope (Zeiss LSM 700), and the intensity was quantified using ImageJ software (NIH). Five samples ($n$ = 5) were prepared for each condition.

*4.9.3. Analysis of ATP Levels in iCell Human Cardiomyocytes.* iCell human cardiomyocytes were seeded into 24-well plates at a density of 50 000 cells/well. After 2 days, the media was switched from the supplier's plating media to the supplier's maintenance media. Then the cells were exposed to either 0 ppm $AgNO_3$ as the control or 0.01 ppm $AgNO_3$ as the sublethal condition along with either no NAC, 5 ppm NAC, or 5 ppm NAC/HA-dopa ($DS_{dopa}$ = 20%). After 12, 24, or 48 h, the ATP levels of the cells were quantified with an ATP colorimetric/fluorometric assay kit (MAK190, Sigma-Aldrich) according to the manufacturer's instructions. The fluorometric assay protocol was followed to maximize sensitivity in the measurement. Following cell lysis and deproteinization with a 10 kDa MWCO spin filter, the samples were diluted several times to ensure the readings are within the linear range of the standard curve generated with the ATP standard provided in the kit. Most trials required a 10−100-fold dilution. The fluorescent readings were measured by using a microplate spectrofluorometer (Infinite 200 PRO, Tecan) with an excitation wavelength of 535 nm and emission wavelength of 587 nm. Five samples ($n$ = 5) were prepared for each condition.

*4.9.4. Analysis of ATP Synthase Activity in iCell Human Cardiomyocytes.* iCell human cardiomyocytes were seeded into 24-well plates at a density of 50 000 cells/well. After 2 days the media was switched from the supplier's plating media to the supplier's maintenance media. Then the cells were exposed to either 0 ppm $AgNO_3$ as the control or 0.01 ppm $AgNO_3$ as the sublethal condition along with either no NAC, 5 ppm NAC, or 5 ppm NAC/HA-dopa ($DS_{dopa}$ = 20%). After 12, 24, or 48 h, the ATP synthase activity was quantified with an ATP synthase enzyme activity microplate assay kit (ab109714, abcam) according to the manufacturer's instructions. The enzyme, ATP synthase, was extracted from cell lysate with the provided detergent and immobilized on a 96-well capture plate. The loading concentration was determined based on the total protein level of the cell lysate. The protein levels were determined with a Pierce BCA Protein Assay Kit (23225, Thermo Scientific). The activity was determined by quantification of the conversion rate of NADH to $NAD^+$ (measured as the decrease in $OD_{340}$/nm) The decrease in absorbance at 340 nm over time was characterized in the linear regime, observed between 10 and 30 min using a microplate spectrofluorometer (Infinite 200 PRO, Tecan). Five samples ($n$ = 5) were prepared for each condition.

*4.9.5. Analysis of iCell Human Cardiomyocyte Contraction Frequency.* iCell human cardiomyocytes were seeded into 24-well plates at a density of 50 000 cells/well. After 2 days the media was switched from the supplier's plating media to the supplier's maintenance media. Then the cells were exposed to either 0 ppm $AgNO_3$ as the control or 0.01 ppm $AgNO_3$ as the sublethal condition along with either no NAC, 5 ppm NAC, or 5 ppm NAC/HA-dopa ($DS_{dopa}$ = 20%). After 12, 24, or 48 h, the contraction for the cell sheets was recorded under an optical microscope (Leica DMIL), and the contraction frequency was determined manually. Five samples ($n$ = 5) were prepared for each condition.

**4.10. *In Vivo* Testing.** *4.10.1. Daphnia magna Maintenance.* *Daphnia magna* were hatched from ephippia purchased from MicroBioTests Inc. (Gent, Belgium) and maintained for more than 10 generations in our laboratory with M4 medium at 21 ± 1 °C. The photoperiod was kept at 16:8 h (light/dark) with a light intensity between 1000 and 1500 lx. Ten adult females were placed in a 2 L beaker filled with 1.5 L M4 medium. The culture medium was changed twice a week. The daphnids were fed daily *ad libitum* with *Chlorella vulgaris* (ca. 1.5 × 108 cells/mL) and a mixture of yeast, cerophyll, and trout chow (YCT) twice a week. *C. vulgaris* was purchased from the Culture Collection of Algae at Cologne University, Germany. The sensitivity of *Daphnia magna* was regularly checked according to ISO 6341 (2012), including potassium dichromate (Sigma-Aldrich, St. Louis, MO, USA) as a reference substance.

*4.10.2. Characterization of Daphnia magna Immobilization.* In all tests, neonates were the third brood of newborns (<24 h) and between the fourth and eighth generations. The acute immobilization test was performed according to OECD guideline 202. Five neonates ($n$ = 5) as a group were placed in six-well culture plates (VWR, Darmstadt, Germany) with 10 mL of ISO media-based test solution. The exposed range of silver ion concentration was 0.0001−0.5 mg/L (ppm). The immobilization and survival were measured after 48 h incubation. The protective effect of NAC and NAC/HA-dopa was also tested against silver-ion exposure. Ten neonates as a group were placed in a 100 mL beaker containing 50 mL of ISO media-based test solution. The exposed concentrations of silver ions were 0.001, 0.002, and 0.008 ppm, respectively. The concentration of NAC and NAC/HA-dopa was set to 5 ppm, and the solutions were prepared in 0.5% DMSO. The immobilization and survival were measured after test solution treatment for 3, 6, 12, 24, and 48 h, respectively.

*4.10.3. Characterization of Daphnia magna Biochemistry Following $AgNO_3$ Exposure.* After exposure according to the designed time, alive neonates were exploited for analysis. Each sample was prepared with 20 neonates ($n$ = 20). Exposed daphnids were gently transferred to E.P. tubes (Sigma-Aldrich) and rinsed with phosphate-buffered saline (PBS; pH 7.4). Then, samples were homogenized in 200 μL of PBS thoroughly by VWR Disposable Pellet Mixers and a Cordless Motor (VWR, Darmstadt, Germany). The homogenized samples were centrifuged under 13 000g at 4 °C for 15 min. Each supernatant was transferred to a new E.P. tube and kept at −80 °C until the assay was conducted. The amount of protein was determined by a Pierce Rapid Gold BCA Protein Assay Kit (Thermo-Scientific, Karlsruhe, Germany). The level of ROS was determined by a cellular ROS assay kit (ab113851, Abcam, Berlin, Germany) based on a 2′,7′-dichlorofluorescein diacetate (DCFDA) reaction. The SOD level was examined by a colorimetric activity kit (EIASODC, Thermo-Scientific) based on the absorbance changes of nitro blue tetrazolium. Relative ATP amount was determined using an ATP bioluminescent assay kit (FLAA, Sigma-Aldrich). In the case of ATPase activity, the ATPase activity assay kit (ab234055, Abcam) was applied for the measurement. The free phosphate ion from the ATPase hydrolysis reacts with malachite green, which generates absorbance changes of free phosphate released (OD650). Therefore, $ddH_2O$ was used for rinsing and homogenization instead of PBS. All assays were followed by the protocol in the assay kits with 20 $\mu$L of the supernatant from the homogenized samples. Fluorescence and absorbance measurements were conducted in the dark using a Spark Multimode Microplate Reader (Tecan Trading AG, Männedorf, Switzerland). The obtained data were normalized by each control sample, consisting of nontreated daphnids.

*4.10.4. Images of Daphnia magna for Fluorescence ROS Assays.* Alive neonates were transferred to the solution of 10 $\mu$M DCFDA in the buffer provided in the ROS assay kit (ab113851, Abcam). After 15 min incubation, the daphnids were washed gently in $ddH_2O$. The visualization was performed using fluorescence microscopy (ZEISS SteREO Discovery V8) with a Plan S 1.0 × FWD 81 mm objective and ZEN 2.6 software. The ImageJ program was exploited for merged images.

*4.10.5. Characterization of Daphnia magna Heart Rate.* The most commonly used end point of toxicity is still to measure death rates of *Daphnia magna*. The immobilization of *Daphnia magna* immobilization was observed at each concentration before counting the heart rate. Lethal concentration ($LC_{50}$) is defined as the concentration of toxic substances that kill 50% of the test organism within a certain exposure period. Survival data were plotted, and $LC_{50}$ values were calculated using a logistic three-parameter curve fitting with Sigmaplot 13.0 software (Systat Software Inc., San Jose, CA, USA). The heart rate was measured to evaluate the influences by exposure to each nanomaterial in triplicate. Neonates hatched within 24 h from the fifth generation of *D. manga* adults were newly prepared on the day of the experiment. Every five neonates were exposed to each concentration level for 3 and 48 h, respectively. The control group was also prepared for comparison with exposure groups under the same conditions without chemical treatment. After exposure, an aliquot of the methyl cellulose solution (4% v/w, Lot No. SLCC9072, Sigma-Aldrich Corp., St. Louis, MO, United States) was treated to fix the individual neonate on the glass plate. We observed heart rate conditions for 1 min using an optical microscope with 4× magnification (model CKX41, Olympus Inc., Tokyo, Japan) and recorded video files. The heart rate was finally counted manually in the play condition of low speed (×0.3).

**4.11. Statistical Analysis.** Averaged data are presented as mean ±95% confidence intervals. The statistical significance between pairs of experimental populations is determined by a nonpaired student's *t* test. $^*p < 0.05$, $^{**}p < 0.01$, and $^{***}p < 0.001$.

## ■ ASSOCIATED CONTENT

### Supporting Information

The Supporting Information is available free of charge at https://pubs.acs.org/doi/10.1021/acsami.2c08889.

$^1$H NMR characterization of HA, dopamine, and HA-dopa; calculated degree of substitution of dopamine ($DS_{dopa}$); FTIR of HA and HA-dopa; fluorescence spectroscopic analysis of 8-aminopyrene-1,3,6-trisulfonic acid trisodium salt (APTS) and APTS conjugation to HA-dopa; metabolic toxicity of $AgNO_3$, NAC, and HA-dopa in H9c2 (2−1) cells; effective concentration studies screening rat cardiomyoblast metabolic efficacy of NAC and NAC/HA-dopa crystals; effective concentration studies screening human cardiomyocyte metabolic efficacy of NAC and NAC/HA-dopa crystals; and daphnid motility and survival following $AgNO_3$ exposure (PDF)

Video showing contraction of iCell cardiac muscle sheet without $AgNO_3$ exposure (MP4)

Video showing contraction of iCell cardiac muscle sheet with $AgNO_3$ exposure and no NAC crystal treatment (MP4)

Video showing contraction of iCell cardiac muscle sheet with $AgNO_3$ exposure and polymer-free NAC crystal treatment (MP4)

Video showing contraction of iCell cardiac muscle sheet with $AgNO_3$ exposure and HA-dopa-stabilized NAC crystal treatment (MP4)

High-speed video showing heart rate of *Daphnia magna* without $AgNO_3$ exposure (MP4)

High-speed video showing heart rate of *Daphnia magna* with $AgNO_3$ exposure and no NAC crystal treatment (MP4)

High-speed video showing heart rate of *Daphnia magna* with $AgNO_3$ exposure and polymer-free NAC crystal treatment (MP4)

High-speed video showing heart rate of *Daphnia magna* with $AgNO_3$ exposure and HA-dopa-stabilized NAC crystal treatment (MP4)

## ■ AUTHOR INFORMATION

### Corresponding Authors

**Hyunjoon Kong** − *Department of Chemical and Biomolecular Engineering and Institute for Genomic Biology, University of Illinois at Urbana—Champaign, Urbana, Illinois 61801, United States; KU-KIST Graduate School of Converging Science and Technology, Korea University, Seoul 02841, Korea;* orcid.org/0000-0003-4680-2968; Email: hjkong06@illinois.edu

**Young Jun Kim** − *Environmental Safety Group, Korea Institute of Science and Technology (KIST−Europe), Saarbrucken 66123, Germany;* Email: youngjunkim@kist-europe.de

### Authors

**Ryan Miller** − *Department of Chemical and Biomolecular Engineering, University of Illinois at Urbana—Champaign, Urbana, Illinois 61801, United States*

**Youngsam Kim** − *Environmental Safety Group, Korea Institute of Science and Technology (KIST−Europe), Saarbrucken 66123, Germany*

**Chang Gyun Park** − *Environmental Safety Group, Korea Institute of Science and Technology (KIST−Europe), Saarbrucken 66123, Germany*

**Chris Torres** − *Department of Chemical and Biomolecular Engineering, University of Illinois at Urbana—Champaign, Urbana, Illinois 61801, United States*

**Byoungsoo Kim** − *Korean Institute of Ceramic Engineering and Technology, Jinju-si 52851, Korea*

**Jonghwi Lee** − *Department of Chemical Engineering and Materials Science, Chung-Ang University, Seoul 06974, Korea;* orcid.org/0000-0003-2336-8695

**David Flaherty** − *Department of Chemical and Biomolecular Engineering, University of Illinois at Urbana—Champaign,* Urbana, Illinois 61801, United States; orcid.org/0000-0002-0567-8481

Hee-Sun Han − Department of Chemistry, University of Illinois at Urbana—Champaign, Urbana, Illinois 61801, United States; orcid.org/0000-0003-3616-291X

Complete contact information is available at:
https://pubs.acs.org/10.1021/acsami.2c08889

### Author Contributions

The manuscript was written through contributions of all authors. All authors have given approval to the final version of the manuscript.

### Notes

The authors declare no competing financial interest.

## ACKNOWLEDGMENTS

This work was supported by the Korea Institute of Science and Technology-Europe (No. CAP-17-01-KIST Europe), partly by the National Science Foundation Research Training Grant (NRT-MBM 1735252), National Science Foundation (NSF-CBET 2032521), National Science Foundation (NSF-CBET 1932192), Department of Defense Vision Research Program under Award (W81XWH-17-1-022), and the Alzheimer Association (2019-AARG-NTF-644507).

## REFERENCES

(1) Lemire, J. A.; Harrison, J. J.; Turner, R. J. Antimicrobial Activity of Metals: Mechanisms, Molecular Targets and Applications. *Nature Reviews Microbiology* **2013**, *11*, 371−384.

(2) Makabenta, J. M. v.; Nabawy, A.; Li, C. H.; Schmidt-Malan, S.; Patel, R.; Rotello, V. M. Nanomaterial-Based Therapeutics for Antibiotic-Resistant Bacterial Infections. *Nature Reviews Microbiology* **2021**, *19*, 23−36.

(3) Kalantari, K.; Mostafavi, E.; Afifi, A. M.; Izadiyan, Z.; Jahangirian, H.; Rafiee-Moghaddam, R.; Webster, T. J. Wound Dressings Functionalized with Silver Nanoparticles: Promises and Pitfalls. *Nanoscale* **2020**, *12*, 2268−2291.

(4) You, C.; Han, C.; Wang, X.; Zheng, Y.; Li, Q.; Hu, X.; Sun, H. The Progress of Silver Nanoparticles in the Antibacterial Mechanism, Clinical Application and Cytotoxicity. *Molecular Biology Reports* **2012**, *39*, 9193−9201.

(5) Wu, C. N.; Fuh, S. C.; Lin, S. P.; Lin, Y. Y.; Chen, H. Y.; Liu, J. M.; Cheng, K. C. TEMPO-Oxidized Bacterial Cellulose Pellicle with Silver Nanoparticles for Wound Dressing. *Biomacromolecules* **2018**, *19* (2), 544−554.

(6) Lim, Y. H.; Tiemann, K. M.; Heo, G. S.; Wagers, P. O.; Rezenom, Y. H.; Zhang, S.; Zhang, F.; Youngs, W. J.; Hunstad, D. A.; Wooley, K. L. Preparation and in Vitro Antimicrobial Activity of Silver-Bearing Degradable Polymeric Nanoparticles of Polyphosphoester-Block-Poly(l-Lactide). *ACS Nano* **2015**, *9* (2), 1995−2008.

(7) Beer, C.; Foldbjerg, R.; Hayashi, Y.; Sutherland, D. S.; Autrup, H. Toxicity of Silver Nanoparticles-Nanoparticle or Silver Ion? *Toxicol. Lett.* **2012**, *208* (3), 286−292.

(8) Yang, L.; Kuang, H.; Zhang, W.; Aguilar, Z. P.; Wei, H.; Xu, H. Comparisons of the Biodistribution and Toxicological Examinations after Repeated Intravenous Administration of Silver and Gold Nanoparticles in Mice. *Sci. Rep.* **2017**, *7* (1), 3303.

(9) Lantagne, D.; Rayner, J.; Mittelman, A.; Pennell, K. Comment on "A re-assessment of the safety of silver in household water treatment: rapid systematic review of mammalian in vivo genotoxicity studies. *Environ. health* **2017**, *16* (1), 121.

(10) Gonzalez, C.; Rosas-Hernandez, H.; Ramirez-Lee, M. A.; Salazar-García, S.; Ali, S. F. Role of Silver Nanoparticles (AgNPs) on the Cardiovascular System. *Arch. Toxicol.* **2016**, *90*, 493−511.

(11) Liu, W.; Worms, I.; Slaveykova, V. I. Interaction of Silver Nanoparticles with Antioxidant Enzymes. *Environmental Science: Nano* **2020**, *7* (5), 1507−1517.

(12) Cameron, S. J.; Hosseinian, F.; Willmore, W. G. A Current Overview of the Biological and Cellular Effects of Nanosilver. *International Journal of Molecular Sciences* **2018**, *19* (7), 2030.

(13) Bondarenko, O.; Juganson, K.; Ivask, A.; Kasemets, K.; Mortimer, M.; Kahru, A. Toxicity of Ag, CuO and ZnO Nanoparticles to Selected Environmentally Relevant Test Organisms and Mammalian Cells in Vitro: A Critical Review. *Arch. Toxicol.* **2013**, *87*, 1181−1200.

(14) Bondarenko, O.; Ivask, A.; Käkinen, A.; Kurvet, I.; Kahru, A. Particle-Cell Contact Enhances Antibacterial Activity of Silver Nanoparticles. *PLoS One* **2013**, *8* (5), 64060.

(15) D'Autréaux, B.; Toledano, M. B. ROS as Signalling Molecules: Mechanisms That Generate Specificity in ROS Homeostasis. *Nat. Rev. Mol. Cell Biol.* **2007**, *8*, 813−824.

(16) Chiarugi, P.; Pani, G.; Giannoni, E.; Taddei, L.; Colavitti, R.; Raugei, G.; Symons, M.; Borrello, S.; Galeotti, T.; Ramponi, G. Reactive Oxygen Species as Essential Mediators of Cell Adhesion: The Oxidative Inhibition of a FAK Tyrosine Phosphatase Is Required for Cell Adhesion. *J. Cell Biol.* **2003**, *161* (5), 933−944.

(17) Schieber, M.; Chandel, N. S. ROS Function in Redox Signaling and Oxidative Stress. *Curr. Biol.* **2014**, *24* (10), 453−462.

(18) Kim, B. S.; Leong, J.; Yu, S. J.; Cho, Y.; Park, C. G.; Kim, D. H.; Ko, E.; Im, S. G.; Lee, J.; Kim, Y. J.; Kong, H. Stimulus-Responsive Anti-Oxidizing Drug Crystals and Their Ecological Implication. *Small* **2019**, *15* (21), 1900765.

(19) Redza-Dutordoir, M.; Averill-Bates, D. A. Activation of Apoptosis Signalling Pathways by Reactive Oxygen Species. *Biochimica et Biophysica Acta - Molecular Cell Research*; Elsevier B.V., 2016; Vol. *1863* (12), pp 2977−2992.

(20) Morimoto, H.; Iwata, K.; Ogonuki, N.; Inoue, K.; Atsuo, O.; Kanatsu-Shinohara, M.; Morimoto, T.; Yabe-Nishimura, C.; Shinohara, T. ROS Are Required for Mouse Spermatogonial Stem Cell Self-Renewal. *Cell Stem Cell* **2013**, *12* (6), 774−786.

(21) Dunnill, C.; Patton, T.; Brennan, J.; Barrett, J.; Dryden, M.; Cooke, J.; Leaper, D.; Georgopoulos, N. T. Reactive Oxygen Species (ROS) and Wound Healing: The Functional Role of ROS and Emerging ROS-Modulating Technologies for Augmentation of the Healing Process. *International Wound Journal* **2017**, *14* (1), 89−96.

(22) Trachootham, D.; Lu, W.; Ogasawara, M. A.; Valle, N. R. del; Huang, P. Redox Regulation of Cell Survival. *Antioxidants and Redox Signaling* **2008**, *10* (8), 1343−1374.

(23) Shen, H.; Pervaiz, S. Reactive Oxygen Species in Cell Fate Decisions. In *Essentials of Apoptosis*; Dong, Z., Yin, X. M., Eds.; Humana Press: Totowa, NJ, 2009.

(24) Soneja, A.; Drews, M.; Malinski, T. Role of Nitric Oxide, Nitroxidative and Oxidative Stress in Wound Healing. *Pharmacology Reports* **2005**, *57*, 108−119.

(25) Collin, F. Chemical Basis of Reactive Oxygen Species Reactivity and Involvement in Neurodegenerative Diseases. *International Journal of Molecular Sciences* **2019**, *20* (10), 2407.

(26) Turrens, J. F. Mitochondrial Formation of Reactive Oxygen Species. *Journal of Physiology* **2003**, *552* (2), 335−344.

(27) Lin, P. W.; Myers, L. E. S.; Ray, L.; Song, S. C.; Nasr, T. R.; Berardinelli, A. J.; Kundu, K.; Murthy, N.; Hansen, J. M.; Neish, A. S. Lactobacillus Rhamnosus Blocks Inflammatory Signaling in Vivo via Reactive Oxygen Species Generation. *Free Radical Biol. Med.* **2009**, *47* (8), 1205−1211.

(28) Hensley, K.; Robinson, K. A.; Gabbita, S. P.; Salsman, S.; Floyd, R. A. Neutrophil-Related Oxidants Drive Heart and Brain Remodeling After Ischemia/Reperfusion Injury. *Fronteirs in Physiology* **2019**, *10*, 1587.

(29) Bertero, E.; Maack, C. Metabolic Remodelling in Heart Failure. *Nature Reviews Cardiology* **2018**, *15*, 457−470.

(30) Patra, R. C.; Swarup, D.; Dwivedi, S. K. Antioxidant Effects of a Tocopherol, Ascorbic Acid and L-Methionine on Lead Induced

Oxidative Stress to the Liver, Kidney and Brain in Rats. *Toxicology* 2001, *162* (2), 81−88.

(31) Zafarullah, M.; Li, W. Q.; Sylvester, J.; Ahmad, M. Review Molecular Mechanisms of N-Acetylcysteine Actions. *Cell Mol. Life Sci.* 2003, *60*, 6−20.

(32) Khalil, I.; Yehye, W. A.; Etxeberria, A. E.; Alhadi, A. A.; Dezfooli, S. M.; Julkapli, N. B. M.; Basirun, W. J.; Seyfoddin, A. Nanoantioxidants: Recent Trends in Antioxidant Delivery Applications. *Antioxidants* 2020, *9* (1), 24.

(33) Zhang, P.; Li, T.; Wu, X.; Nice, E. C.; Huang, C.; Zhang, Y. Oxidative Stress and Diabetes: Antioxidative Strategies. *Frontiers of Medicine* 2020, *14*, 583−600.

(34) Newman, A.; Knipp, G.; Zografi, G. Assessing the Performance of Amorphous Solid Dispersions. *J. Pharm. Sci.* 2012, *101* (4), 1355−1377.

(35) Kakran, M.; Sahoo, N. G.; Tan, Y. W.; Li, L. Ternary Dispersions to Enhance Solubility of Poorly Water Soluble Antioxidants. *Colloids Surf., A* 2013, *433*, 111−121.

(36) Fan, N.; He, Z.; Ma, P.; Wang, X.; Li, C.; Sun, J.; Sun, Y.; Li, J. Impact of HPMC on Inhibiting Crystallization and Improving Permeability of Curcumin Amorphous Solid Dispersions. *Carbohydr. Polym.* 2018, *181*, 543−550.

(37) Kumari, A.; Yadav, S. K.; Pakade, Y. B.; Singh, B.; Yadav, S. C. Development of Biodegradable Nanoparticles for Delivery of Quercetin. *Colloids Surf., B* 2010, *80* (2), 184−192.

(38) Kaur, R.; Rajput, R.; Nag, P.; Kumar, S.; Singh, M. Synthesis, Characterization and Evaluation of Antioxidant Properties of Catechin Hydrate Nanoparticles. *Journal of Drug Delivery Science and Technology* 2017, *39*, 398−407.

(39) de Cristo Soares Alves, A.; Mainardes, R. M.; Khalil, N. M. Nanoencapsulation of Gallic Acid and Evaluation of Its Cytotoxicity and Antioxidant Activity. *Materials Science and Engineering C* 2016, *60*, 126−134.

(40) Rakotoarisoa, M.; Angelov, B.; Espinoza, S.; Khakurel, K.; Bizien, T.; Angelova, A. Cubic Liquid Crystalline Nanostructures Involving Catalase and Curcumin: BioSAXS Study and Catalase Peroxidatic Function after Cubosomal Nanoparticle Treatment of Differentiated SH-SY5Y Cells. *Molecules* 2019, *24* (17), 3058.

(41) Rakotoarisoa, M.; Angelov, B.; Espinoza, S.; Khakurel, K.; Bizien, T.; Drechsler, M.; Angelova, A. Composition-Switchable Liquid Crystalline Nanostructures as Green Formulations of Curcumin and Fish Oil. *ACS Sustainable Chem. Eng.* 2021, *9* (44), 14821−14835.

(42) Aldini, G.; Altomare, A.; Baron, G.; Vistoli, G.; Carini, M.; Borsani, L.; Sergio, F. N-Acetylcysteine as an Antioxidant and Disulphide Breaking Agent: The Reasons Why. *Free Radical Research* 2018, *52* (7), 751−762.

(43) Rushworth, G. F.; Megson, I. L. Existing and Potential Therapeutic Uses for N-Acetylcysteine: The Need for Conversion to Intracellular Glutathione for Antioxidant Benefits. *Pharmacology and Therapeutics* 2014, *141* (2), 150−159.

(44) Zhitkovich, A. N-Acetylcysteine: Antioxidant, Aldehyde Scavenger, and More. *Chem. Res. Toxicol.* 2019, *32* (7), 1318−1319.

(45) Tkaczyk, A.; Bownik, A.; Dudka, J.; Kowal, K.; Ślaska, B. Daphnia Magna Model in the Toxicity Assessment of Pharmaceuticals: A Review. *Sci. Total Environ.* 2021, *763*, 143038.

(46) Damásio, J.; Tauler, R.; Teixidó, E.; Rieradevall, M.; Prat, N.; Riva, M. C.; Soares, A. M. V. M.; Barata, C. Combined Use of Daphnia Magna in Situ Bioassays, Biomarkers and Biological Indices to Diagnose and Identify Environmental Pressures on Invertebrate Communities in Two Mediterranean Urbanized and Industrialized Rivers (NE Spain). *Aquatic Toxicology* 2008, *87* (4), 310−320.

(47) Siciliano, A.; Gesuele, R.; Pagano, G.; Guida, M. How Daphnia (Cladocera) Assays May Be Used as Bioindicators of Health Effects? *Journal of Biodiversity & Endangered Species* 2015, *1* (5), 005.

(48) Minkov, V. S.; Boldyreva, E. V.; Drebushchak, T. N.; Gorbitz, C. H. Stabilizing structures of cysteine-containing crystals with respect to variations of temperature and pressure by immobilizing amino acid side chains. *CrystEngComm* 2012, *14*, 5943−5954.

(49) Kumar, S. S.; Nangia, A. A New Conformational Polymorph of N-Acetyl-l-Cysteine. the Role of S-H···O and C-H···O Interactions. *CrystEngComm* 2013, *15* (33), 6498−6505.

(50) Kong, H. J.; Lee, K. Y.; Mooney, D. J. Nondestructively Probing the Cross-Linking Density of Polymeric Hydrogels. *Macromolecules* 2003, *36* (20), 7887−7890.

(51) Schmidt, J. J.; Jeong, J. H.; Chan, V.; Cha, C.; Baek, K.; Lai, M. H.; Bashir, R.; Kong, H. Tailoring the Dependency between Rigidity and Water Uptake of a Microfabricated Hydrogel with the Conformational Rigidity of a Polymer Cross-Linker. *Biomacromolecules* 2013, *14* (5), 1361−1369.